Nanoelectromechanical Resonators: Bridging Microwave Optomechanical Circuits and Phonon-Cavity Systems

Xin Zhou

Habilitation à Diriger des Recherches

Nanoelectromechanical Resonators: Bridging Microwave Optomechanical Circuits and Phonon-Cavity Systems

Author: Xin Zhou

Affiliation: CNRS, IEMN

September 09, 2024

Keywords: **microwave optomechanics, nanoelectromechanical membrane resonators, phonon-cavity, scanning microwave microscopy, mapping mode, computing, sensing**

Committee:

Dr. Katia Grenier, DR	CNRS-LAAS	Rapportrice
Dr. Bernard Legrand, DR	CNRS-LAAS	Rapporteur
Dr. Anthony Ayari, DR	CNRS-ILM	Rapporteur
Dr. Olivier Arcizet, DR	CNRS-NEEL	Examinateur
Dr. Ashwin A. Seshia, Professor	University of Cambridge	Examinateur
Dr. Eddy Collin, DR	CNRS-NEEL	Membre invité
Dr. Didier Theron, DR	CNRS-IEMN	Guarantee

Acknowledgements

As I begin to write this strange manuscript, I am very grateful to my former supervisors and colleagues during my postdoctoral and Ph.D. periods, especially Shunri Oda, Koji Ishibashi, Daniel Esteve, Denis Vion, and Eddy Collin. They provided me with invaluable research conditions and resources that helped me develop a range of scientific skills, including nanofabrication, microwave engineering, analytical computing, simulation and instrumentation. They taught me the attitude and the approach to understand physics. More importantly, they have given me confidence and shown me many examples of the courage to push forward when the going gets tough.

Abstract

This manuscript presents an overview of my research activities in the study of the multimode coupling in microwave optomechanical circuits and phonon-cavity nanomechanics, and the topics that will be pursued based on current advances. The studies start with the experimental realisation of a microwave optomechanical platform to investigate on-chip phonon thermometry in a single-tone pumping scheme and optomechanically induced transparency/amplifications in a double-tone driving scheme. The same physics and experimental techniques are then transferred in investigations of mechanical phonon-phonon interactions in phonon-cavity nanomechanics, consisting of two distinct and capacitively coupled membrane resonators, analogous to optomechanics. To understand how energy is coherently transferred in coupled multimodes, semi-classical and classical models of microwave optomechanical circuits and phonon-cavity systems have been developed according to different drive configurations. In addition, by integrating microwave interferometry with a scanning tip, I have experimentally extended the applications of scanning microwave microscopy to image mechanical vibration modes of a membrane. Using these mode coupling techniques, the energy, in the form of phonons, can be coherently transferred between the scanning tip and its coupled membrane resonators. These experimental results are based not only on our efforts in theoretical analysis, but also on advanced microwave setups and novel silicon nitride membrane nanoelectromechanical systems developed by using advanced nanofabrication techniques. These achievements and accumulated techniques allow ongoing research activities to focus on the exploration of computational functions and quantum sensing in coupled mechanical resonators and microwave optomechanical systems.

Contents

1. Introduction

I start studying physics in high school by learning the basic properties of a harmonic oscillator. Throughout various physics textbooks, single or coupled oscillators are frequently employed as ideal models to elucidate a wide array of systems in both physics and engineering. For instance, the theoretical modeling of modern quantum superconducting circuits and Josephson junction qubits is grounded in the principles of harmonic oscillators with additional nonlinearities. Micro/nanoelectromechanical resonators (MEMS/NEMS) have been recognized for decades for their diverse sensing applications. Beyond their role as sensors, these resonators serve as ideal models and multifunctional elements, particularly in hybrid mechanical resonator systems and coupled nanomechanical networks. Their inherent weak nonlinearities present opportunities for exploring advanced signal processing and computing functions. Additionally, these devices enable the coupling of mechanical degrees of freedom with external signals extending beyond wavelength. Therefore, the potential applications of MEMS/NEMS are vast and **should not and will not be confined to sensor applications alone**. This is what motivates me to work in the field of microwave optomechanical devices (a nanoelectromechanical resonator coupled with a microwave cavity) and coupled nanoelectromechanical systems.

This manuscript is used to apply for a "habilitation à diriger des recherches" (HDR) in France. Therefore, it is written to give a brief overview of my primary research (after obtaining a permanent position) in the highly interdisciplinary fields: microwave optomechanics and nanoelectromechanics. The total scientific part of the manuscript is about 60 pages, according to "advices". It consists of 4 chapters and an additional chapter for introducing the research topic that will be carried out in the next few years. Each chapter starts with a general introduction to the background of the subject and includes small parts of the derived analytical calculations to guide and understand our experimental results.

The chapter 2 focuses on developing microwave optomechanical devices, including the theoretical part of using electrical circuit model to describe classical nature of the microwave optomechanical properties, and the experiment of microwave optomechanical thermometry in a single-tone driving scheme and optomechanically induced amplification/transparency in a double-tone driving scheme. Measurement results are well described by our electrical circuit model. The chapter 3 presents an analogy of an optomechanical system using two capacitively coupled distinct membrane resonators. By implementing double-tone techniques, we are able to coherently manipulate the energy transfer between the resonators using parametric coupling based on electrostatic forces. In addition, the unique device scheme allows us to observe "anti-damping" effects in both vibrating membranes that cannot be achieved in typical microwave optomechanical device. The experimental results have been well fitted using our derivations of electromechanical phonon-cavity model. It provides a method for routing signals in complex coupled multimode systems. The chapter 4 shows a novel platform based on scanning microwave microscopy integrated with microwave interferometry. The scanning tip, which acts

as a suspended top gate, is used to drive and spatially map the tiny displacements of a membrane resonator, without the need for physical contact with the sample. In addition, we can coherently control the energy cycling between the tip vibration mode and the membrane mode. This novel platform not only extends the applications of scanning microwave microscopy, but it also offers a new method of investigating mechanical properties of the resonator when it is integrated in a complex electrical circuit. All of these research achievements, which are presented in chapter 2, 3, and 4, are based on the low noise microwave readout setup and the silicon nitride membrane resonators that I have developed in IEMN clean-room. The details of setup and nanofabrication process are given in the 5 chapter.

These progresses made in research to date serve as critical building blocks for the exploration of computational and sensing functionalities within coupled NEMS/MEMS networks. These advances have led me to initiate investigations into neuron-inspired computing through the use of the nonlinearity in the coupled NEMS networks within a microwave optomechanical platform. To date, we have made progress in reservoir computing by creating coupled virtual nodes (analogous to coupled neural networks) in a single NEMS. In addition, we have already demonstrated the potential of thermal sensing using a single nanoelectromechanical resonator. The focus is now on extending thermal sensing capabilities to coupled networks and exploring quantum sensing methods. More details of the perspective are described in chapter 6.

So far, I have supervised two PhD students and both of them obtained degrees, including Dylan CATTIAUX (co-supervised by Eddy Collin) and Hao XU (co-supervised by Didier Theron). Each student had more than 3 international publications with me. One of the students won the GDR-MecaQ 2021 thesis prize. Now, I am supervising the 3rd PhD student Loic FLIS (co-supervised by Didier Theron) from the Sep. 2023 to now. I have supervised three postdocs, two of whom have gone on to become researchers. I also supervised two Masters students, one of whom had a scientific publication under my supervision. Besides supervising students, I also coordinated and participated in 9 research projects. Several international and national collaborations have been established, including fruitful collaborations with NEEL in Grenoble, LOMA in Bordeaux, the University of Southampton in UK, attached to the European microkelvin platform (EMP) network, and so on. In addition, since 2018, I have been serving as a member of the scientific committee of GDR-mecaQ for several years and coordinated this GDR annual meeting in Lille in 2023. More details have been included in my CV.

I am happy to share my little personal pleasure: all the parameters of the nanofabrication process used to make the capacitively coupled membranes, as well as all the Mathematica/Python codes I wrote for the calculations associated with this manuscript. If you are interested, please contact me: xin.zhou@cnrs.fr

2. Microwave optomechanical circuits: probe and readout nanomechanical resonator through the cavity force

In the last decades, great scientific successes have been achieved in cavity optomechanics, which uses laser photons to explore the interaction between optical fields and mechanical motion [1]. Cavity optomechanics allows to cool down suspended micro-mirrors and to excite cold atom clouds through the radiation-pressure effect, which enables the investigation of mechanical systems in the quantum regime [2, 3, 4]. Optical forces also offer a method to enhance the resolution of nano-mechanical sensors through the optical spring effect [5]. Optomechancial platforms are thus both *model systems* containing rich physics to be explored [1], but also *unique sensors* able to detect extremely tiny forces/displacements, especially in the quantum regime as foreseen in the 80's [6]. Besides, the amazing sensitivity of optomechanics for displacement detection lead to the *tour de force* detection of the long-thought gravitational waves [7].

Over the past 20 years, circuit quantum electrodynamics (cQED) has made significant advances in the control and measurement of quantum states using superconducting circuits, leading to breakthroughs in quantum computing and quantum information processing [8, 9, 10, 11, 12]. These achievements have enabled more precise manipulation of qubits, which has facilitated the development of scalable quantum technologies. Inspired by the achievements of the QED, researchers eventually started to use microwave photons confined in a superconducting resonator to probe micro/nano-mechanical oscillators, leading to the new experimental field of *microwave optomechanics* [13]. It inherits the abundant physical and technological properties emerging from cavity optomechanics, and benefits from the capabilities of microwave circuit designs. Especially, low temperature experiments performed in this wavelength range allow the use of

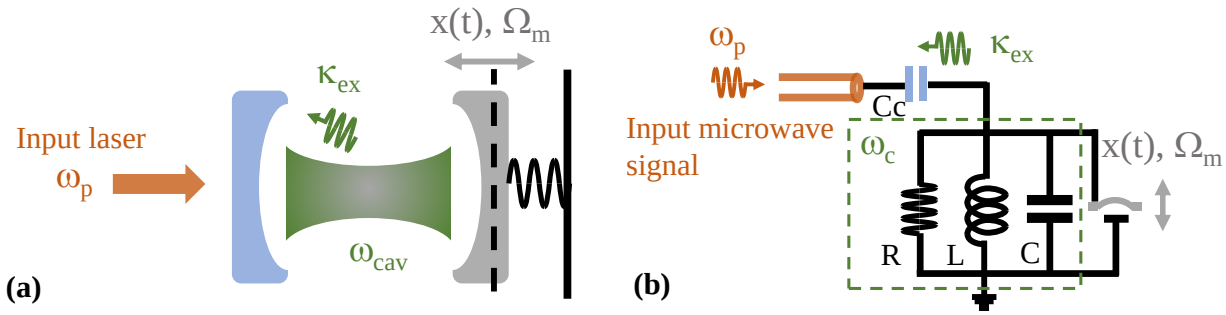

Figure 2.1: Schematic diagram comparing a generic optomechanical system (top) and an electrical *RLC* circuit (bottom). See text for the color code.

quantum electronics components such as Josephson parametric amplifiers [14]. Building on microwave optomechanical schemes, sideband cooling of mechanical motion down to the quantum ground state and entanglement of massive mechanical oscillators have been recently achieved [15, 16]. Moreover, microwave optomechanical platforms with cavity-enhanced sensitivity have been built, squeezing the classical thermal fluctuations of the mechanical element [17, 18, 19]. The latter clearly demonstrates that optomechanics is not only reserved for frontiers experiments in quantum mechanics, but represents also a new resource for classical devices with novel applications.

2.1. Basic principle of optomechanics

2.1.1. Cavity optomechanics, described by Hamiltonian formulation

Within circuit QED, Hamiltonian formulations adapted to various quantum circuits have been developed using the mathematical toolbox of quantum mechanics. This has been achieved by quantizing (i.e. promoting to operators) variables of electrical engineering (e.g. voltage, current) and building the corresponding generic quantum circuit theory [20, 9, 21]. The propagation of signals in coplanar waveguides (CPW) is characterized by the movement of bosonic modes, such as photons, while localized modes describe signal propagation in RLC resonators. To effectively describe driving fields and detected signals, input-output theory and quantum noise formalisms are essential, particularly within the framework of the quantum version of the fluctuation-dissipation theorem as applied to superconducting circuits [22, 23]. This theoretical framework draws upon works such as those by Gardiner and Clerk [24, 25]. Quantum electric circuit theory allows for the modelling of nonlinear features and dissipation, which are critical for understanding device performance and advancing circuit design. Notably, quantum-limited Josephson amplifiers are modeled by treating Josephson junctions as tunable nonlinear inductors, as demonstrated in studies by Vijay and Zhou [26, 27]. The quantum electrodynamic (QED) formalism has been elaborated upon for mechanical transducers, effectively bridging concepts from quantum optics and quantum electronics. In most theoretical work, formalisms based on quantum operators have been widely used to describe optomechanical properties.

If we use Hamiltonian to describe two uncoupled modes, the optical (ω_{cav}) and mechanical (Ω_m) modes, it can be represented by two harmonic oscillators:

$$\hat{H}_0 = \hbar\omega_{\mathrm{cav}}\hat{a}^\dagger\hat{a} + \hbar\Omega_m\hat{b}^\dagger\hat{b}, \tag{2.1}$$

where both $\hat{a}$ and $\hat{b}$ are quantum operators, with relations of $[\hat{a}, \hat{a}^\dagger] = 1$ and $[\hat{b}, \hat{b}^\dagger] = 1$. The total photon number confined in the cavity n_c and the total phonon number n_m occupied by the mechanical oscillator are defined by $\hat{a}^\dagger\hat{a} = n_c$ and $\hat{b}^\dagger\hat{b} = n_m$. For a mechanical oscillator, it is easy to link the mechanical displacement x and momentum p with the operators $\hat{b}$ and $\hat{b}^\dagger$,

with

$$\hat{b} = \sqrt{\frac{k}{2\hbar\Omega_m}}\hat{x} + i\frac{1}{\sqrt{2m\hbar\Omega_m}}\hat{p},$$
$$\hat{b}^\dagger = \sqrt{\frac{k}{2\hbar\Omega_m}}\hat{x} - i\frac{1}{\sqrt{2m\hbar\Omega_m}}\hat{p}. \tag{2.2}$$

In the case of the optical cavity with a movable end mirror, as shown in Fig.2.1, the parametric coupling exists between the optical cavity and the mechanical vibration. Because the cavity mode will be modulated by the mechanical displacement,

$$\omega_{\rm cav}(x) \approx \omega_{\rm cav} + x\frac{\partial\omega_{\rm cav}}{\partial x}. \tag{2.3}$$

The coupling rate between the optical mode and the mechanical mode is therefore given by

$$G = -\frac{\partial\omega_{\rm cav}}{\partial x}, \tag{2.4}$$

through the definition of the optical frequency shift per displacement. Then, the Hamiltonian for a description of two coupled modes in optomechanics arrives The coupling rate between the optical mode and the mechanical mode is therefore given by

$$\hat{H}_c = \hbar\omega_{\rm cav}\hat{a}^\dagger\hat{a} + \hbar\Omega_m\hat{b}^\dagger\hat{b} + \hbar G\hat{a}^\dagger\hat{a}(\hat{b}+\hat{b}^\dagger)\sqrt{\frac{\hbar}{2m\Omega_m}}, \tag{2.5}$$

with $\hat{x} = (\hat{b}+\hat{b}^\dagger)\sqrt{\frac{\hbar}{2m\Omega_m}}$. The mechanical zero-point fluctuation amplitude is defined to be x_{zep}=$\sqrt{\frac{\hbar}{2m\Omega_m}}$, the mechanical displacement generated by quantum noise. Thus, the other definition of coupling rate g_0, so called single photon coupling rate, arrives $g_0 = Gx_{zep}$. The Eq.2.5 can be re-written in form of g_0,

$$\hat{H}_c = \hbar\omega_{\rm cav}\hat{a}^\dagger\hat{a} + \hbar\Omega_m\hat{b}^\dagger\hat{b} + \hbar g_0\hat{a}^\dagger\hat{a}(\hat{b}+\hat{b}^\dagger). \tag{2.6}$$

Based on the input-output theory, the dynamic equation of the operator is given by

$$\frac{\partial\hat{a}}{\partial t} = \frac{1}{i\hbar}[\hat{a},\hat{H}_c] - \frac{\kappa_t}{2}\hat{a} + \sqrt{\kappa_c}\hat{a}_{in} \tag{2.7}$$

Here, the κ_t represents the total damping rate of the optical cavity, including internal (κ_i) and external (κ_c) damping rate, $\kappa_t = \kappa_c + \kappa_i$. The κ_c denotes the energy exchange rate between the external and internal cavity components. The operator $\hat{a}$ defines the energy confined inside the cavity. To understand the output signal of the cavity $\hat{a}_{out}$ that will be detected, the input-output theory is mandatory, described by

$$\hat{a}_{in}(t) + \hat{a}_{out}(t) = \sqrt{\kappa_t}\hat{a}(t). \tag{2.8}$$

If we consider $\hat{a}$ = a(t)$e^{-i\omega t}$ and put into Eq.2.6-2.7, the cavity field amplitude $\hat{a}_{in}$ becomes

$$\frac{\partial\hat{a}}{\partial t} = -\frac{\kappa_t}{2}\hat{a} + i[(\omega-\omega_{cav}) + G\hat{x}]\hat{a} + \sqrt{\kappa_c}\hat{a}_{in} \tag{2.9}$$

To linearize the Hamiltonian in Eq.2.5, an approximation has been made to split the cavity field into an average coherent amplitude $< \hat{a} > = \bar{\alpha}$ and a fluctuation term $\delta\hat{a}$

$$\begin{aligned} \hat{a} &= \bar{\alpha} + \delta\hat{a}, \\ \hat{x} &= \bar{x} + \delta\hat{x}. \end{aligned} \tag{2.10}$$

Therefore, the static solution gives the steady state, with

$$\begin{aligned} \bar{\alpha} &= -\frac{\sqrt{\kappa_c}}{i(\Delta - G\bar{x}) - \frac{\kappa_t}{2}} a_{in}, \\ \bar{x} &= -\frac{\hbar G\bar{\alpha}^2}{m\Omega^2}. \end{aligned} \tag{2.11}$$

The intra-cavity average photon number is $n_c = |\bar{\alpha}|^2$. Now, we consider a force generated by the electromagnetic fields confined inside the cavity, F = -$\hbar G\hat{a}^\dagger\hat{a}$. Its small fluctuation δF = -$\hbar G\bar{\alpha}(\delta a + \delta a^*)$. Now, we take expressions of δa and δx into account in order to present the back-action effect,

$$\dot{\delta}a(t) = (i\Delta - \kappa_t/2)\delta a(t) - iG\bar{a}\delta x(t), \tag{2.12}$$

and

$$\ddot{\delta}x(t) + \gamma_{\rm m}\dot{\delta}x(t) + \Omega_{\rm m}^2\delta x(t) = -\frac{\hbar G\bar{a}}{m_{\rm eff}}\left(\delta a(t) + \delta a^*(t)\right). \tag{2.13}$$

Note that $\dot{\delta}a(t)$ will be fourier transferred into frequency domain, to be $-i\Omega\delta a(\Omega)$. In the rotation frame, the solution of δa is given by

$$\begin{aligned} \delta a(\Omega) &= \frac{G\bar{a}}{(\Delta + \Omega) + i\kappa_t/2}\delta x(\Omega), \\ \delta a^*(\Omega) &= \frac{G\bar{a}}{(\Delta - \Omega) - i\kappa_t/2}\delta x(\Omega). \end{aligned} \tag{2.14}$$

Then, the small variations of back-action force δF are given by

$$\begin{aligned} \delta F_{\rm rp}(\Omega) =& -\hbar G\bar{a}\left(\delta a(\Omega) + \delta a^*(\Omega)\right) \\ =& -\hbar G^2\bar{n}_{\rm c}\left(\frac{\Delta + \Omega}{(\Delta + \Omega)^2 + (\kappa/2)^2} + \frac{\Delta - \Omega}{(\Delta - \Omega)^2 + (\kappa/2)^2}\right)\delta x(\Omega) \\ &+ i\hbar G^2\bar{n}_{\rm c}\left(\frac{\kappa_c/2}{(\Delta + \Omega)^2 + (\kappa_t/2)^2} - \frac{\kappa_c/2}{(\Delta - \Omega)^2 + (\kappa_t/2)^2}\right)\delta x(\Omega). \end{aligned} \tag{2.15}$$

If we compare Eq.2.15 with Eq.2.13, it is evident that δF modify the susceptibility of the coupled mechanical resonator. The real part contributes to the modifications of mechanical resonance frequency Ω_m^2 and the imaginary part gives the modifications of the initial mechanical damping rate γ_m,

$$\begin{aligned} \delta\gamma &= \frac{\hbar G^2\bar{n}_{\rm c}}{2m_{\rm eff}\Omega_m}\left(\frac{\kappa_c}{(\Delta + \Omega_m)^2 + (\kappa/2)^2} - \frac{\kappa_c}{(\Delta - \Omega_m)^2 + (\kappa_t/2)^2}\right), \\ \delta\Omega^2 &= \frac{\hbar G^2\bar{n}_{\rm c}}{m_{\rm eff}}\left(\frac{\Delta + \Omega_m}{(\Delta + \Omega_m)^2 + (\kappa_t/2)^2} + \frac{\Delta - \Omega_m}{(\Delta - \Omega_m)^2 + (\kappa_t/2)^2}\right). \end{aligned} \tag{2.16}$$

Then, the mechanical damping rate becomes $\gamma_{eff} = \gamma_m + \delta\gamma$, so-called optomechanical damping effect. While, the new resonance frequency modified to be $\Omega^2_{eff} = \Omega^2_m + \delta\Omega^2$, so-called optical spring effect [1]. This semi-classic method has been widely used for deducing the formulas of optomechanical systems. To describe the quantum features in optomechanics, the general method is to write input to be in the form of the quantum noise, instead of using input signal, in Eq.2.7. More attention should be paid to the order of the operators when calculating correlations. In addition, although the Hamiltonian formulation is used to describe the typical optomechanical system, the semi-classical method is widely used for derivations to linearize and simplify the Hamiltonian.

2.1.2. Microwave optomechanics, modeled by a LCR circuit

For microwave optomechanics, although its basic principle and relevant applications are not restricted to quantum mechanics, today the full classical circuit model has not yet been presented, despite useful pioneering discussions [1]. Therefore, the theoretical framework used for all experiments, even if purely classical in nature, is still based on the Hamiltonian derived from quantum optics [1]. This means that the physical description is overly complex, losing sight of the real (classical) nature of most properties, and that the connection between circuit parameters and optomechanical properties is not clearly identified, whereas **it is a need for design and optimization**.

2.1.3. Equivalent circuits, input-output expression, dynamics equation, and calculation approachs

To build the LCR circuit model, I start to consider two widely used equivalent circuits for microwave optomechanics in current experiments, with different input and output designs, as shown in Fig. 2.2. The microwave cavity consists of a simple LC_kR_{in} circuit. The coupled nanomechanical resonator, acting as a movable capacitor, $C_g(x)$, is coupled to this LC_kR_{in}. In Fig. 2.2 (a) we show the electric schematic of a bi-directional coupling: the RLC resonator couples evanescently to a nearby transmission line with an effective capacitance Cc [28, 15, 29]. If we define the damping rate the cavity as κ_{ex}, then $\kappa_{ex}/2 = \kappa_L = \kappa_R$. In Fig. 2.2 (b), only one port is connected to the device, requiring thus the use of a specific nonreciprocal component (e.g. like a circulator) to separate the drive signal from the response (reflection mode) [30]. This is equivalent to scheme (a), with $\kappa_{ex} = \kappa_L$ and $\kappa_R = 0$.

The second key point is to build the input-output expression for the circuit model. We shall consider in the following a single port configuration, e.g Fig. 2.2 (b), the extension to the other models being straightforward from what has been said above. Whenever necessary, this correspondence will be explicitly discussed. The circuits shown in Fig. 2.2 are a combination of transmission lines (the coaxial cables) and lumped elements (RLC, Z_0 impedances, and source). The first step of the modelling is thus to get rid of the coaxial elements, in order to model an

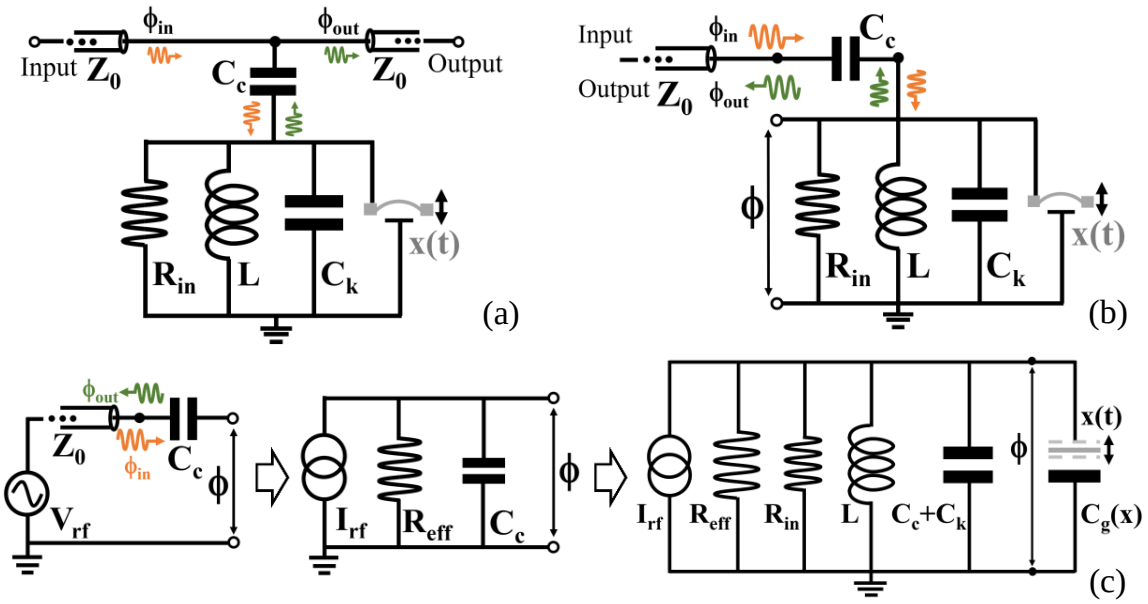

Figure 2.2: Schematic diagram comparing a generic microwave optomechanical *LCR circuit (a) readout in transmission method, (b) readout in reflection method. (c) equivalent parallel circuit, from the voltage source to a current source*

ideal lumped circuit. To start with, we consider the source $V_{\rm rf}$ which generates the incoming wave ϕ_{in}, with $\phi(t) = \int^t V(t')dt'$. In schemes (b) of Fig. 2.2, the drive port is terminated by an (almost) open circuit since the coupling capacitance is very small ($C_c\omega\, Z_0 \ll 1$). The incoming wave is thus almost fully reflected, and the standing wave voltage on the input capacitor is $V_d \approx 2V_{\rm rf}$ [31]. On the other hand for scheme (b), the transmission line is almost unperturbed by the coupling element C_c, and the incoming wave travels toward the output port (almost) preserving its magnitude; on the coupling capacitor we have $V_d \approx V_{\rm rf}$.
Applying Norton's theorem, we transform the series voltage source input circuit into a parallel RC, which drives a total current I_d across it. This is shown in Fig. 2.2 (b), with finally the total loaded RLC resonator design. The effective components of the Norton drive circuit are defined from the real and imaginary parts of the complex admittance $Y_c(\omega) = [Z_0 + 1/(iC_c\omega)]^{-1}$, in the limit $C_c\omega\, Z_0 \ll 1$ (weak coupling):

$$R_{ex} = \frac{1}{(\omega_c C_c)^2\, Z_0}, \tag{2.17}$$

with the approximation $\omega \approx \omega_c$. Here, the i is the *imaginary* unit. The $\Re[Y_c(\omega)]$ contributes to the R_{ex}, with $\Re[Y_c(\omega)] = 1/R_{ex}$. The imaginary part of Y_c, with $\Im[Y_c(\omega)] \approx i\omega_c C_c$ links the I_d and the voltage. The current I_d flowing into the resonator then writes:

$$I_d \approx i\omega_c C_c\, V_d. \tag{2.18}$$

The detected voltage is calculated from the current flowing through the amplifier's impedance

Z_0. For circuits Fig. 2.2 (b), this simply leads to:

$$V_{\text{out}} \approx -\omega_c^2 C_c Z_0 \, \phi, \tag{2.19}$$

assuming again $\omega \approx \omega_c$. (We do not report here the contribution from the incoming wave that eventually travels to the amplifier.) For circuit (a), the evanescent coupling leads to a loading composed of two impedances Z_0 in parallel (half of the signal is fed back to the voltage source):

$$V_{\text{out}} \approx -\omega_c^2 C_c \frac{Z_0}{2} \, \phi. \tag{2.20}$$

The **classical dynamics equation** that describes this problem writes:

$$\begin{aligned} &\frac{d}{dt}\left((C_c + C_k + C_g[x])\,\frac{d\phi}{dt}\right) + \left(\frac{1}{R_{ex}} + \frac{1}{R_{in}}\right)\frac{d\phi}{dt} + \frac{1}{L}\phi \\ &= I_d + I_{\text{noise}}. \end{aligned} \tag{2.21}$$

It should be noted that the value of ϕ is the biased flux inside the microwave cavity, not the detected value. In the experiment, the readout value should be calculated through input-output theory, based on the Eq. 2.19 or Eq.2.20, depending on the numbers of the coupled port used in the readout circuits.

2.1.4. Damping rate of the microwave cavity

In the following, we will consider small motion, which is always true in optomechanical circuits. Because the typical displacement of a nanomechanical resonator is in the order of a few nm. And the coupling capacitance between the movable element and its gate, $C_g(x)$, is always much smaller than the coupling capacitance C_c. We therefore write $C_g(x) \approx C_g(0) + x(t) \times dC_g(0)/dx$, defining the total (static) capacitance $C_t = C_c + C_k + C_g(0)$ [32, 33]. $C_g(0)$ corresponds to the contribution of the mobile element when at rest, while C_c comes from the slight "leakage" of the cavity mode into the coaxial lines. The rates are then defined from the electronic components:

$$\kappa_t = \kappa_{ex} + \kappa_c, \tag{2.22}$$

$$\kappa_{ex} = \frac{1}{R_{ex} C_t} = \frac{(\omega_c C_c)^2 \, Z_0}{C_t}, \tag{2.23}$$

$$\kappa_{in} = \frac{1}{R_{in} C_t}. \tag{2.24}$$

In the two-port case, one simply defines R_1 and R_2 leading to $1/R_{ex} = 1/R_1 + 1/R_2$, and similarly $1/R_t = 1/R_{ex} + 1/R_{in}$; we write the corresponding quality factors $Q_i = \omega_c/\kappa_i$ (with $i = in, ex, t$). Besides, the microwave resonance of the loaded RLC circuit is given by $\omega_c = 1/\sqrt{LC_t}$. From Eq. 2.22 to Eq. 2.24, it is straightforward to see that if one would like to control

the energy leaking rate between external and internal cavity, the readout speed of internal filed ϕ, the value of C_c should be carefully considered in the circuit design. Besides, it also can be engineered by modifying the coupled impedance environment, the value Z_0. The internal damping rate of the circuit is modeled through R_{in}, leading to a κ_{in} decay rate (measuring the decay toward internal degrees of freedom). Usually, the internal damping is caused by the material losses. For instance, in order to reduce the microwave dissipation from the dielectric layer on a silicon substrate, researchers prefer to choose quartz or sapphire substrate for the fabrication of superconducting quantum circuits. The total decay rate of the microwave mode is then $\kappa_t = \kappa_{ex} + \kappa_{in}$.

2.1.5. Coupling rate in the microwave optomechanical circuits

When we look at the definition of the coupling rate in optomechanics, Eq.2.4, it is not difficult to find the relation between the coupling rate G and the coupling capacitance C_g in microwave optomechanical system.

$$\begin{aligned} G &= -\frac{\partial \omega_c}{\partial x}, \\ &= -\frac{1}{\sqrt{L}}\frac{\partial C_t}{\partial x}, \\ &= \frac{\omega_c}{2C_t}\frac{\partial C_g(x)}{\partial x}. \end{aligned} \tag{2.25}$$

Therefore, in order to increase the coupling rate value G in the circuit, it is necessary to have a higher coupling capacitance between the mechanical resonator and the cavity.

2.1.6. Calculation approaches

The drive current writes $I_d(t) = \frac{1}{2} I_p e^{-i\omega_p t} + \text{c.c.}$ with ω_p the frequency at which the microwave pumping is applied and I_p its (complex) amplitude. We introduce the frequency detuning $\Delta = \omega_p - \omega_c$. From Eq. (2.18), I_p is derived from the input voltage drive amplitude V_p. Note that impedances are expressed in the standard electronics language assuming $A_0 \exp(+i\omega t)$ time-dependencies. The writing should be adapted for full $A_0 \exp(-i\omega t) + \text{c.c.}$ expressions. The mechanical displacement is written as $x(t) = \frac{1}{2} x_0(t) e^{-i\Omega_m t} + \text{c.c.}$ with $x_0(t)$ the (complex) motion amplitude translated in frequency around Ω_m, the mechanical resonance frequency of the movable element. This amplitude is a stochastic variable: the *Brownian motion* of the moving element thermalized at temperature T_m, in the absence of the back-action from the circuit.

The terms where motion $x(t)$ multiplies flux $\phi(t)$ in Eq. (2.21) then generate harmonics at $\omega_n = \omega_p + n\,\Omega_m$, with $n \in \mathbb{Z}$: this phenomenon is known as *nonlinear mixing*. We can thus find an exact solution using the *ansatz*:

$$\phi(t) = \sum_{n=-\infty}^{+\infty} \phi_n(t) = \sum_{n=-\infty}^{+\infty} \frac{1}{2} \mu_n(t) e^{-i(\omega_p + n\Omega_m)t} + \text{c.c.}, \tag{2.26}$$

when injected in Eq. (2.21) generates a system of coupled equations for the μ_n (complex) amplitudes. In order to match the decomposition, the white noise component is thus naturally written as $I_{\text{noise}} = \sum_n \frac{1}{2}\delta I_n(t) e^{-i(\omega_p + n\Omega_m)t} + \text{c.c.}$ with $\delta I_n(t)$ the (complex) amplitude translated at frenquency $\omega_p + n\,\Omega_m$. From the full comb, we thus keep only $n = -1, 0, +1$ which we rename in 'l' (low), 'p' (pump) and 'h' (high) respectively for clarity. Here, the mechanical resonance frequency Ω_m is much smaller than the resonance frequency of microwave cavity ω_c, $\Omega_m \ll \omega_c$, which is considered as a standard experimental condition in microwave optomechanics.

With the approximation $\omega_l \approx \omega_p \approx \omega_h \approx \omega_c$, we solve the Eq.2.21 by considering the cavity is pumped at the frequency ω_p. Then, the flux amplitudes inside the cavity acting on the mechanical oscillator are:

$$\begin{aligned}
\mu_p(t) &= +\frac{i}{2}\left(\frac{I_p}{\omega_c C_t} + \frac{\delta I_p(t)}{\omega_c C_t}\right)\chi_p, \\
\mu_l(t) &= +\frac{i}{2}\left(G\, x_0^*(t)\mu_p(t) + \frac{\delta I_l(t)}{\omega_c C_t}\right)\chi_l, \\
\mu_h(t) &= +\frac{i}{2}\left(G\, x_0(t)\mu_p(t) + \frac{\delta I_h(t)}{\omega_c C_t}\right)\chi_h,
\end{aligned} \tag{2.27}$$

having defined:

$$\chi_p = \frac{1}{-i\Delta + \frac{\kappa_t}{2}}, \tag{2.28}$$

$$\chi_l = \frac{1}{-i\,(\Delta - \Omega_m) + \frac{\kappa_t}{2}}, \tag{2.29}$$

$$\chi_h = \frac{1}{-i\,(\Delta + \Omega_m) + \frac{\kappa_t}{2}}, \tag{2.30}$$

the *cavity susceptibilities* associated to each spectral component. The two satellite signals μ_l and μ_h at $\omega_p \pm \Omega_m$ are generated by the pump tone μ_p. When the pump tone is at the resonance frequency $\omega_p = \omega_c$, it yields $\Delta = 0$, giving $\mu_l = \mu_h$. We call it as green pump. While, when the $\Delta \neq 0$ but with $\Delta \approx \Omega_m$, one of the generated satellite signals around ω_c has the higher amplitude. The other one is suppressed due to out-of-the-cavity bandwidth.

2.1.7. Classical features of optomechanics in single-tone driving scheme

Back-action of cavity forces: optical spring effect and damping effect

From Eq.2.28 to Eq.2.30, a cavity force F_0 can be generated because of the pump tone, $\delta F_0(\omega) = +i\frac{G}{2}\left[\delta I_h(\omega)\,\mu_p^*\,\chi_h - \delta I_l^*(\omega)\,\mu_p\,\chi_l^*\right]$. Together with the Langevin force, they will modulate the mechanical susceptibilities.

$$x_0(\omega) = \chi_m(\omega)\left[L_0(\omega) + \delta F_0(\omega)\right], \tag{2.31}$$

where we have defined:

$$\chi_m(\omega) = \frac{1}{2m\Omega_m\left(-\omega - i\frac{\Gamma_m}{2}\right) + \Sigma}, \tag{2.32}$$

$$\Sigma = -i\frac{G^2}{\omega_c}\left(\frac{C_t\omega_c^2\left|\mu_p\right|^2}{2}\right)\left[\chi_h - \chi_l^*\right]. \tag{2.33}$$

Taking real and imaginary parts of Σ, we see from Eq. (2.32) that the optomechanical interaction is responsible for a frequency shift $\delta\Omega_m$ and an additional damping term $\Gamma_{\rm opt}$:

$$\begin{aligned}\delta\Omega_m &= G^2\frac{1}{\omega_c\left(2m\Omega_m\right)}\left(\frac{C_t\omega_c^2\left|\mu_p\right|^2}{2}\right)\times \\ &\left[\frac{\Delta+\Omega_m}{(\Delta+\Omega_m)^2+(\frac{\kappa_t}{2})^2}+\frac{\Delta-\Omega_m}{(\Delta-\Omega_m)^2+(\frac{\kappa_t}{2})^2}\right],\end{aligned} \tag{2.34}$$

$$\begin{aligned}\Gamma_{\rm opt} &= G^2\frac{1}{\omega_c\left(2m\Omega_m\right)}\left(\frac{C_t\omega_c^2\left|\mu_p\right|^2}{2}\right)\times \\ &\left[\frac{\kappa_t}{(\Delta+\Omega_m)^2+(\frac{\kappa_t}{2})^2}-\frac{\kappa_t}{(\Delta-\Omega_m)^2+(\frac{\kappa_t}{2})^2}\right].\end{aligned} \tag{2.35}$$

It is consistent with Eq.2.16, derived by using quantum operators in section 2.1.1. But compared to Hamiltonian formalism, this model of an electric circuit combines many parameters that are accessible to experiments. Moreover, the derivations directly tell the truth that the cavity force in optomechanics is a kind of electrostatic force and is generated by frequency conversions in microwave optomechanics.
Besides, the energy E_c stored in the microwave resonator writes:

$$\begin{aligned}E_c &= \frac{C_t\omega_c^2\left|\mu_p\right|^2}{2} = P_{in}\,\kappa_{ex}\left|\chi_p\right|^2, \\ &= n_c\,\hbar\,\omega_c.\end{aligned} \tag{2.36}$$

From Eq.2.34 and Eq.2.35, it is easy to see that both coupling rate G and photon numbers n_c play important role in optomecanical effects. In the microwave optomechanical system, the high quality factor of the microwave cavity and the high capacitive coupling value C_g between the cavity and the coupled mechanical resonators are both significant factors to consider.

Sideband asymmetry

As discussed above (see Eq.2.27), when the microwave cavity is pumped, two satellite signals will be generated. Their values not only rely on the pump amplitude μ_p but also on the noise δI_i. This noise can be quantum noise or thermal noise. An interesting point is that the cross-correlations between the cavity noise and the mechanical motion will contribute to the output

of the spectrum, as described in Eq.2.37 and Eq.2.38.

$$\begin{aligned} S_{\mu_l}(\omega) &= |\mu_p|^2 G^2 \frac{S_{x_0}(\omega)}{4} |\chi_l|^2 + \frac{R_t S_{\delta I_n}}{4} \frac{\kappa_t}{C_t \omega_c^2} |\chi_l|^2 \\ &\quad + \frac{|\mu_p|^2 G^2 \kappa_t}{2\omega_c} \left[i(\chi_m^* \chi_l - \chi_m \chi_l^*) \right] \frac{R_t S_{\delta I_n}}{4} |\chi_l|^2, \end{aligned} \tag{2.37}$$

$$\begin{aligned} S_{\mu_h}(\omega) &= |\mu_p|^2 G^2 \frac{S_{x_0}(\omega)}{4} |\chi_h|^2 + \frac{R_t S_{\delta I_n}}{4} \frac{\kappa_t}{C_t \omega_c^2} |\chi_h|^2 \\ &\quad + \frac{|\mu_p|^2 G^2 \kappa_t}{2\omega_c} \left[i(\chi_m \chi_h - \chi_m^* \chi_h^*) \right] \frac{R_t S_{\delta I_n}}{4} |\chi_h|^2. \end{aligned} \tag{2.38}$$

The last terms in Eq.2.37 and Eq.2.38 correspond to cross-correlations between the cavity noise current and the motion. Besides, the output of the spectrum also relies on the cross-correction between the cavity noise and the noise of the detection background, as shown in Eq.2.39 and Eq.2.40.

$$\begin{aligned} S_{\mu_l, \delta V_l}(\omega) &= + \frac{2(\omega_c C_c Z_0)}{\omega_c C_t} \left[\chi_l + \chi_l^* \right] \frac{R_{ex} S_{\delta I_n}}{4} \\ &\quad + |\mu_p|^2 G^2 (\omega_c C_c Z_0) \left[i(\chi_l^2 \chi_m^* - \chi_l^{*2} \chi_m) \right] \frac{R_{ex} S_{\delta I_n}}{4}, \end{aligned} \tag{2.39}$$

$$\begin{aligned} S_{\mu_h, \delta V_h}(\omega) &= + \frac{2(\omega_c C_c Z_0)}{\omega_c C_t} \left[\chi_h + \chi_h^* \right] \frac{R_{ex} S_{\delta I_n}}{4} \\ &\quad + |\mu_p|^2 G^2 (\omega_c C_c Z_0) \left[i(\chi_h^2 \chi_m - \chi_h^{*2} \chi_m^*) \right] \frac{R_{ex} S_{\delta I_n}}{4}. \end{aligned} \tag{2.40}$$

These products from cross-correlation can be recast into apparent stochastic force, back affecting the mechanical motions. For instance, we define a temperature for the detection port as $R_{ex} S_{I_{\text{noise}}} = R_{ex} S_{\delta I_n}/4 = k_B T_{ex}$ and the background noise becomes $2k_B T_{ex}$. The cross-correlations between the detection background and the cavity noise give extra force noise $\delta F_{ex\,l}$ and $\delta F_{ex\,h}$.

For the "blue" pumping scheme, only the 'l' sideband is measurable in the sideband-resolved limit. Injecting $\Delta = +\Omega_m$ in the above mentioned equations, we obtain:

$$S_{\delta F_{ex\,l}} = 2m\Gamma_{\text{eff}}\, k_B \left(+2T_c - T_{ex} \right) \frac{\Omega_m}{\omega_c}, \tag{2.41}$$

with T_c and T_{ex} the temperatures of the cavity and the detection port respectively.
Similarly for the "red" pumping scheme, with $\Delta = -\Omega_m$ and looking at the 'h' sideband we have:

$$S_{\delta F_{ex\,h}} = 2m\Gamma_{\text{eff}}\, k_B \left(+T_{ex} - 2T_c \right) \frac{\Omega_m}{\omega_c}. \tag{2.42}$$

In both expressions, $\Gamma_{\text{eff}} = \Gamma_m + \Gamma_{\text{opt}}$ but Γ_{opt} is different: negative for the "blue" scheme, and positive for the "red" one. However, for low drive powers $\Gamma_{\text{opt}} \approx 0$ and $\Gamma_{\text{eff}} \approx \Gamma_m$. In this case, a very simple result emerges: the two apparent force noises are opposite, a result referred to in the literature as *sideband asymmetry* [1, 34]. But here, the feature is *purely classical*, and by

no means a signature of quantum fluctuations.

In the case of a "green" pumping scheme, $\Delta = 0$ and both sidebands can be measured at the same time. The resulting expressions for the cross-correlation apparent stochastic force components are:

$$\begin{aligned} S_{\delta F_{ex\,l}} &= 2m\Gamma_m\, k_B\,(+T_{ex})\,\frac{\Omega_m}{\omega_c}, \\ S_{\delta F_{ex\,h}} &= 2m\Gamma_m\, k_B\,(-T_{ex})\,\frac{\Omega_m}{\omega_c}, \end{aligned} \tag{2.43}$$

again in the sideband-resolved limit. Eqs. (2.43) are very similar to Eqs. (2.41,2.42): again the two forces are opposite, but this time they depend only on T_{ex}.

Let us consider the case of an ideally thermalized system were $T_c = T_{ex} = T_m$. Then in the limit $\Gamma_{\text{opt}} \approx 0$, sideband asymmetry measured by comparing the 'l' peak in "blue" pumping Eq. (2.41) with the 'h' peak in "red" Eq. (2.42) gives strictly the same result as the direct comparison of the two sidebands Eqs. (2.43) observed with a "green" scheme. Besides, the sideband asymmetry effect simply renormalizes the observed mechanical temperature by $T_m \to T_m(1+\Omega_m/\omega_c)$ on the 'l' side, and by $T_m \to T_m(1-\Omega_m/\omega_c)$ on the 'h' side; since $\Omega_m/\omega_c \ll 1$, this effect can be safely neglected in this case. One needs to artificially create a situation where $T_m \ll T_{ex}$ to make the sideband asymmetry detectable (e.g. by sideband cooling the mechanical mode, and injecting noise through the microwave port) [34]. As soon as $T \to 0$ K, the classical picture breaks down and all features should be interpreted in the framework of quantum mechanics; including sideband asymmetry. A recent experiment has demonstrated very good agreement with this formalism, without free parameters [35].

Classical analogue

The main optomechanical results applying to the "green" pumping scheme ($\omega_p \approx \omega_c$) are compared in Tab. 2.1 in the classical and quantum regimes. Here, the δE is the output of energy for the cavity. Once we want to make a straightforward comparison, the energy in classical states can be re-written in the form of photon numbers, with a universal expression $\delta E = n_c\hbar\omega$. The key point revealed by the classical modelling is that all features have a classical analogue; only the $T \to 0$ K *quantities* are a true signature of quantumness, which highlights the importance of calibrations in all conducted experiments. More details are present in our previous publication [36].

2.2. Microwave single-tone manipulations: on-chip optomechanical thermometry

Primary thermometers are those whose temperature can be calculated directly from the reading of a physical parameter using a known physical law, which does not need to be calibrated by

Quantity	Quantum limit	Classical limit
$S_x^{imp} S_{\delta F}$	$\frac{\kappa_t}{\kappa_{ex}}\hbar^2/4$	$\frac{1}{2}\frac{\kappa_t}{\kappa_{ex}} k_B T_c \, \delta E/(\omega_c^2)$
$\mathcal{S}_{ig}$	$\propto x_{zpf}^2/2$	$\propto k_B T_m/(2\, m\Omega_m^2)$
$\mathcal{N}_{oise}$	$\propto x_{zpf}^2$	$\propto \sqrt{\delta E \, k_B T_c}/(\sqrt{2}\, m\Omega_m \omega_c)$
$\mathcal{S}_{ig}/\mathcal{N}_{oise}$	1/2	$k_B T_m \omega_c/(\sqrt{2}\sqrt{\delta E \, k_B T_c}\, \Omega_m)$

Table 2.1: $S_x^{imp} S_{\delta F}$ product, signal $\mathcal{S}_{ig}$, noise $\mathcal{N}_{oise}$ and signal-to-noise ratio in the quantum and classical limits (the latter are given at the optimal n_c for the "green" pumping scheme; δE energy detection resolution and T_c cavity temperature, see text).

other thermometers. They are needed to calibrate thermometers and are of interest to industry. Today, the cryostat market is growing rapidly, driven by increased demand for cryostats in healthcare (nuclear magnetic resonance imaging), the aerospace industry and scientific instrumentation. However, the cryogenic industry and research activities are facing the problem of the lack of suitable primary thermometers with the following properties: a wide working temperature range (10 mK- 300 K), high accuracy, and integration in a small space. Today, most cryostats have to be equipped with several different thermometers, which not only take up a significant amount of space, but also require additional wiring and complex calibration.

The operating temperature range of the primary thermometer is determined by the physics on which it is based. For example, the operating range of the Coulomb blockade primary thermometer is limited in the low and intermediate Coulomb blockade regime (typically < 20K) and the superconducting quantum interference device (SQUIDs) thermometer is limited by the transition temperature of the superconducting material [37]. In addition, some of these well-developed primary thermometers require additional protection (e.g. anti-magnetic for the SQUID thermometer) or are sensitive to magnetic fields (e.g. Pt NMR), making them difficult to integrate on-chip.

Microwave optomechanical circuits offer a method to read out the phonon occupation numbers n_m of the coupled nanomechanical resonators through cavity force. The basic principle is to use a "light" microwave signal pumping system at frequency $\omega_p = \omega_c + \Omega_m$, called blue sideband pumping. Based on the RLC circuit model (see Eq. 2.27), the spectrum existing inside the

Devices	Type	Working range	Integration with on-chip	Cost	Sensitive to magnetic field
Resistor thermometer	Secondary	100 mK to RT	Difficult	Low	No
Coulomb Blockade thermometer	Primary	20 mK to 20 K	Easy	Low	No
SQUID thermometer	Primary	ULT to 2K	Possible	Low	Yes
Pt NMR thermometer	Primary	ULT to 80 mK	Difficult	High	Yes
MOP thermometer	Primary	ULT to RT	Easy	Low	No

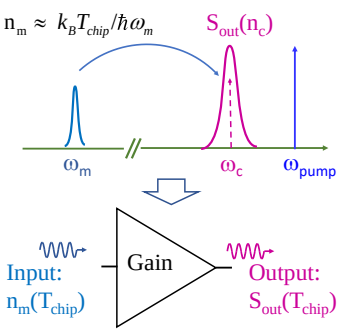

Figure 2.3: Left: comparison of this project with the state of the art. 'Secondary' means that they must be calibrated by other thermometers, 'ULT' is T< = 30mK. Right: schematic diagram of microwave optomechanical phonon thermometry.

cavity at the frequency around ω_c is given by:

$$\begin{aligned} S_{\mu_l}(\omega) = |\mu_p|^2 G^2 \frac{S_{x_0}(\omega)}{4} |\chi_l|^2 + \frac{R_t S_{\delta I_n}}{4} \frac{\kappa_t}{C_t \omega_c^2} |\chi_l|^2 \\ + \frac{|\mu_p|^2 G^2 \kappa_t}{2\omega_c} [i(\chi_m^* \chi_l - \chi_m \chi_l^*)] \frac{R_t S_{\delta I_n}}{4} |\chi_l|^2 , \end{aligned} \tag{2.44}$$

with

$$2\pi \int S_{x_0} d\omega = x_{zpf}^2 n_m \frac{\Gamma_m}{\Gamma_{\text{eff}}}. \tag{2.45}$$

It is easy to see that the phonons from the MEMS has been amplified by the microwave pump amplitude μ_p, as shown in Figure 2.3. The gain of this amplification can be obtained by measuring the noise spectral density corresponding to different pump powers. Consequently, the initial number of phonons n_m will be obtained by removing the gain of the optomechanical amplification from the measured output signals. To assess accuracy, we will compare the n_m measured by our thermometer with temperatures measured by other commercial thermometers, such as resistors.

Figure 2.4 shows the measurement results of a microwave thermometry, measured between 20 mK and 1 K. In the blue sideband pumping scheme, the phonon occupation numbers of the mechanical resonator increase with increasing pump amplitude. We, therefore, observe that the integrated area of S_{x_0} increases as shown in the Fig.2.4. Through careful calibrations of the gain in blue sideband pumping, The true detected temperature T_{mode} can be read, consistent with the cryostat temperature. However, as the pump amplitude increases in the red sideband pumping scheme, the measured areas of the spectral density S_{x_0} increase initially and then become saturated. The more numbers of phonons will be pumped out at the higher pump power, yielding the weaker signal for detection, whose readout is limited by the sensitivity of the detection chain, e.g. the amplifier.

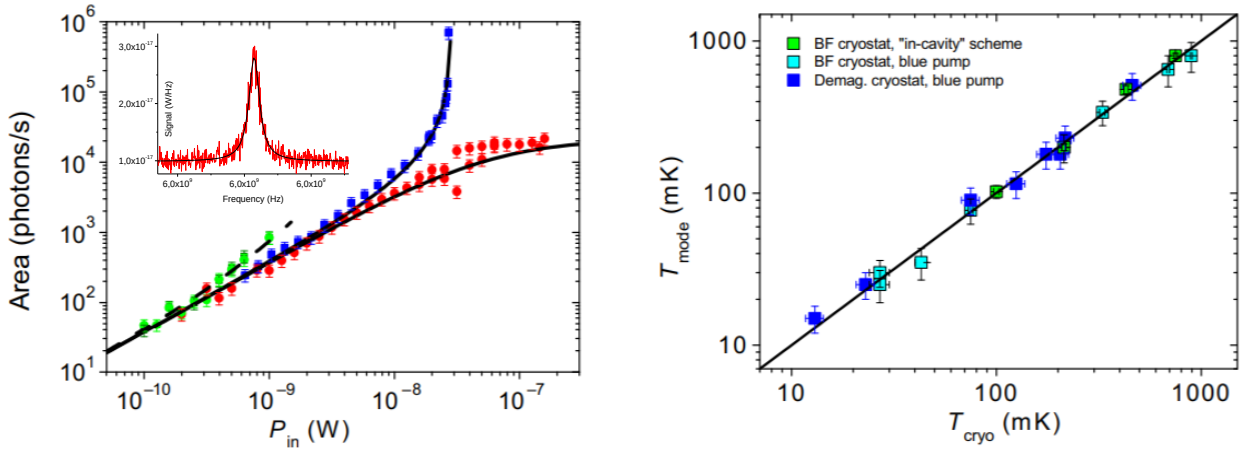

Figure 2.4: Left: Area of measured spectrum density of the nanomechanical resonator as a function of pump power P_{in}, corresponding to different pump schemes. The inset figure is one example of the measured spectrum density of a nanomechanical resonator in a microwave optomechanical circuit. Right: The mode temperature as a function of cryostat temperature. These data have been published by author [29].

2.3. Microwave double-tone manipulations: optomechanically induced transparency and amplifications

The microwave optomechanical systems also give access to the double-tone operations, probing the microwave cavity and pumping the cavity at its sideband. To describe this operation, we can re-write Eq.2.21 to be

$$\frac{I_s}{C_{\mathrm{T0}}} = \left(1 + \frac{2G}{\omega_c}X\right)\ddot{\phi} + \left(k_T + \frac{2G}{\omega_c}\frac{\mathrm{d}}{\mathrm{d}t}X\right)\dot{\phi} + \omega_c^2\phi, \tag{2.46}$$

with solutions in the form of $\phi[\omega] = \frac{\mu}{2}e^{-\mathrm{i}\omega t} + \frac{\mu^*}{2}e^{\mathrm{i}\omega t}$ and $X[\Omega] = \frac{\mu_x}{2}e^{-\mathrm{i}\Omega t} + \frac{\mu_x^*}{2}e^{\mathrm{i}\omega t}$. Note that the internal filed in the cavity ϕ should be re-written in a form of $\phi = \phi_s[\omega_s] + \phi_p[\omega_p]$, in which $\phi[\omega_s]$ is generated by the sideband pump I_p and will create interference with the probe signal (I_s) at the frequency ω_s. When the interferences become constructive, the probe signal will be amplified. For destructive interference, the probe signal will be suppressed due to destructive interference. The solution of Eq.2.46 is given by

$$\begin{aligned}\mu_p &= \frac{I_{\mathrm{p}}}{C_{\mathrm{t0}}\left({\omega_{\mathrm{c}}}^2 - {\omega_{\mathrm{p}}}^2 - \mathrm{i}\omega_{\mathrm{p}}k_t\right)} \\ \mu_s^* &= \frac{I_{\mathrm{s}}\omega_{\mathrm{c}} + G{\mu_x}^*{\mu_p}^*\omega_{\mathrm{p}}\omega_{\mathrm{s}}C_{\mathrm{t0}}}{\omega_{\mathrm{c}}C_{\mathrm{t0}}\left({\omega_{\mathrm{c}}}^2 - {\omega_{\mathrm{s}}}^2 + \mathrm{i}\omega_{\mathrm{s}}k_t\right)}\end{aligned} \tag{2.47}$$

It gives a back-action force f_{back} to the mechanical resonator

$$f_{\mathrm{back}} = \omega_p G C_{t0}\left(\frac{\mu_s{\mu_p}^*}{2}\mathrm{e}^{\mathrm{i}\Omega t} + \frac{{\mu_s}^*\mu_p}{2}\mathrm{e}^{-\mathrm{i}\Omega t}\right). \tag{2.48}$$

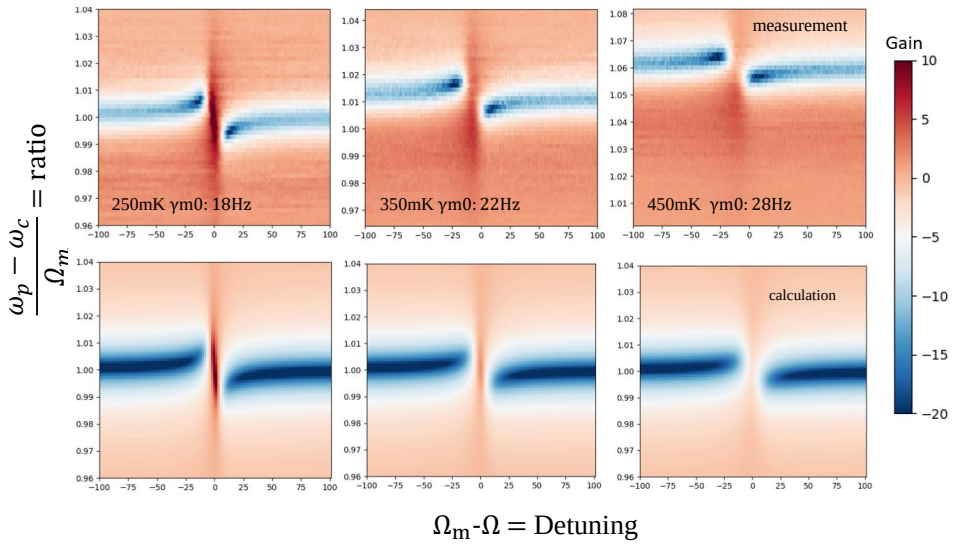

Figure 2.5: 2D plots the signal gain in blue sideband pumping scheme, corresponding to both signal and pump frequency detuning. Top figures show the measurement results, down figures are the calculation results. In calculation, we used experimental parameters: $g_0 = 0.8$ Hz, $\omega_c/(2\pi)$ =5.98 GHz, $\Omega_m/(2\pi)$ ∼3.7 MHz, $\kappa_t/(2\pi) \sim 10^5$ Hz, pump power=-65 dBm, signal=-110 dBm, γ_{m0} is the initial bandwidth of NEMS.

This cavity force will play the same role as in the single-tone driving scheme (see Eq.2.31), modulating the mechanical damping rate and resonance frequency. When we consider the nanomechanical resonator is driven by the cavity force, μ_x arrives

$$\mu_x = \frac{\mu_s^* \mu_p}{m_{eff}} \frac{\omega_p G C_{t0}}{2\Omega\left(\Omega_m - \Omega - \frac{i\gamma_m}{2}\right)}, \tag{2.49}$$

with $\Omega = \omega_p - \omega_s$, with $\Omega > 0$ in the blue sideband pumping condition and $\Omega < 0$ for the red sideband configuration. When one puts expressions of μ_p and μ_s in Eq.2.47 to Eq.2.49, we get expression of mechanical displacement μ_x in this two-tone driving scheme

$$\begin{aligned}\mu_x = &- \frac{G P_{in} S_{in} \omega_p}{m_{eff}\,\Omega(i\gamma_m + 2\Omega - 2\Omega_m) C_{t0}\left(\omega_c^2 - \omega_p^2 - i\omega_p k_T\right)\left(\omega_c^2 - \omega_s^2 + i\omega_s k_T\right)} \\ &\times \frac{1}{\left(1 + \frac{G^2 P_{in} \mu_p^* \omega_p^2 \omega_s}{m_{eff}\,\Omega\,\omega_c (i\gamma_m + 2\Omega - 2\Omega_m)\left(\omega_c^2 - \omega_p^2 - i\omega_p k_T\right)\left(\omega_c^2 - \omega_s^2 + i\omega_s k_T\right)}\right)}.\end{aligned} \tag{2.50}$$

$$\begin{aligned}Gain = &1 - \frac{i k_c}{\omega_c - \omega_s + i\frac{k_t}{2}} \pm \\ &\frac{i g_0^2 k_c n_c}{\left(\frac{i\gamma_m}{2} + \Omega - \Omega_m\right)\left(\omega_c - \omega_s + \frac{i k_t}{2}\right)\left(\left(\omega_c - \omega_s + \frac{i k_t}{2}\right) \pm \frac{g_0^2 n_c}{\left(\frac{i\gamma_m}{2} + \Omega - \Omega_m\right)}\right)}\end{aligned} \tag{2.51}$$

If we re-write the output as a signal gain, μ_{out}/μ_{in} (see Eq.2.51. The symbol "$\pm$" is taken to be "-" for the red sideband pump tone and "+" for the blue sideband pump tone.), it is easy to see the effects of interference between the cavity susceptibility and the mechanical susceptibility. Such kind interference is generated from the microwave photons created by frequency mixing between the probe signal inside the cavity and the pump tone at the cavity's sideband. This interference has also been observed in two coupled nanomechanical resonators at room temperature (see section3.1.1). In the experiment, the resonance frequency of microwave cavity is set as a frequency reference, with $\Delta = \omega_p - \Omega_s$, and the probe signal is sweep through taking the pump tone as the reference ($\Omega = \omega_p - \omega_s$), giving $\omega_c - \omega_s = \Omega - \Delta$. Figure 2.5 shows both the measurement and calculation results based on Eq.2.51, in a blue sideband pumping scheme. The results can be fitted quite well by this analytical expression, derived in the electric circuit model. A small signal gain can be generated because of the constructive interference between the probe tone and the pump tone. As the mechanical damping rate γ_m increases with temperature, the efficiency of these constructive perturbations decreases, resulting in a decrease in gain. Note that if the cavity is pumped at its red sideband, destructive interference will occur, resulting in transparency of the probe signal [38, 39, 40].

2.4. Summary of chapter-2

We have introduced a generic classical electric circuit model that mirrors the conventional quantum treatment of optomechanics. Through this analytical framework, connections between circuit parameters and quantum optics quantities are established, crucial for design and optimization purposes. These two approaches are interchangeable under the condition that temperatures are sufficiently high for both mechanical and electromagnetic degrees of freedom. This classical electric circuit model has been exploited to design microwave optomechanical circuits and fit experimental results [29]. It not only adapts to a single-tone driving scheme, but can also be upgraded to a multi-tone driving configuration. In addition to theoretical modelling, on-chip thermometry and optomechanically induced amplification/transparency have been experimentally demonstrated. The development of microwave on-chip thermometry will solve the problem of lack of thermometry in the ultra-low temperature range (T $<$ 10 mK). The working temperature of this on-chip thermometry is limited by the superconducting material (Nb thin film). Nevertheless, with a microwave cavity capable of operating across a broad temperature spectrum, the concept of microwave optomechanical thermometry becomes applicable across various temperature ranges, from room temperature to ultra-low temperatures, leveraging techniques such as 3D cavity design. This is the reason that we also developed 3D microwave cavity (see section 5.1.3). The optomechanically induced amplification/transparency can be further exploited for microwave tunable amplifiers/filters. Different driving schemes also demonstrate the flexibilities of optomechanical operations.

3. Coupled membrane nanoelectromechanical resonators, for phonon-cavity nanoelectromechanics

Micro- and nano-electromechanical systems, allowing mechanical displacements to couple with electrical and optical signals, are extensively studied for various applications and fundamental research [41, 42, 43, 44, 45]. The specific features of tiny scale and high quality factor resonances are attractive for sensing applications [46, 47, 48, 49, 50]. Their intrinsic nonlinearity and mechanical transduction design have been implemented for developing logic gates [51, 52], radio frequency (rf) amplifiers [53] and memory nodes [54]. In recent years, the study of mode coupling, which exists between different mechanical modes in a single system but also between different resonators, attracts great research interests. Because they allow to transmit information between mechanical modes [55, 56] and to filter signals in different frequency bands through controlling transfers of energy [57]. In addition to these applied possibilities, such devices can also be viewed as model systems to implement mechanical analogues of some other phenomena [58]. Coupled mechanical modes are crucial for extending the signal of nanomechanical resonators to coupled NEMS/MEMS networks, in order to explore multifunctional nanoelectromechanical systems.

As such, one of the successful examples exploiting mechanical mode coupling is the concept of "phonon-cavity" [59, 60], inspired by recent achievements in optomechanics. Optomechanics, which studies interactions between the mechanical vibrations and photons confined in a cavity, offers a powerful platform for many engineering applications, from sensing (e.g. detecting thermal Brownian motion) to the generation of mechanical self-sustained oscillations, and even the storage of light [61, 62, 39]. In order for the two coupled mechanical modes to exploit the rich physics available with optomechanics, the phonon-cavity scheme is built by implementing the mode with the higher resonance frequency Ω_1 as a phonon cavity in analogy with the optical/microwave one, and then pumping it with a signal at frequency $\sim \Omega_1 \pm \Omega_2$. Here, Ω_2 is the resonance frequency of the other mode. The concept of phonon-cavity not only enables the two coupled mechanical modes to inherit those interesting functions of optomechanics, but also further enriches existing optomechanical applications, in both classical and potentially the quantum regime [60, 63, 64, 65].

Up to now, in most phonon-cavity schemes, the coupling is created between different mechanical modes with a single resonator by means of an intrinsic nonlinearity, or between different resonators by using physical connections to transmit a displacement-induced tension [60, 55, 46, 66, 67, 68]. However, mechanical coupling design yields implementation complexities in optimizing the coupling between distinct and distributed resonators, and poses a challenge for electromechanical devices desiring higher resonance frequencies and flexible tun-

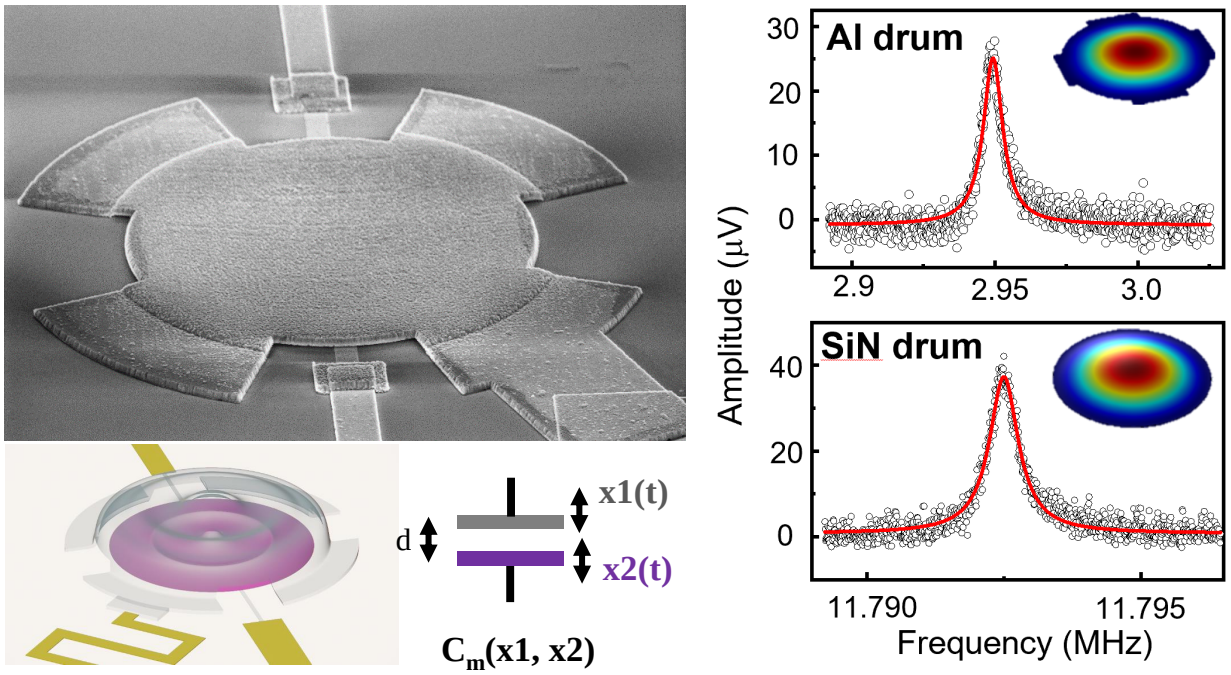

Figure 3.1: Left: SEM image of the device consisting of an Al membrane on top capacitively coupled to a silicon nitride membrane below. Bottom: Schematic diagram of the device structure and the corresponding equivalent capacitor consisting of two movable parallel plates. Right: mechanical responses of both membrane resonators, measured at room temperature.

ability. Compared to mechanical coupling designs, electrostatic coupling schemes are widely implemented in diverse electrical integrated systems. It allows to implement the coupling of distributed resonators experiencing nano-scale displacements, but also to drive/detect independently each resonator of the coupled system [69, 70]. However, it is still challenging to achieve directly coupled distinct mechanical resonators via capacitive coupling, especially for compact schemes.

Therefore, we have developed a new nanoelectromechanical scheme, consisting of an Al drum suspended on top of a silicon nitride membrane drum, as shown in Fig3.1. Both resonators can be driven and detected independently. The device fabrication process is introduced in chapter 5 section5.2. This device design offers an opportunity to study mode coupling. Moreover, it provides the advantage of low power manipulations as the vibration membranes exhibit a high coupling rate with external circuits. This is especially evident in microwave optomechanical systems [71].

In this chapter, I present coherent energy transfers between two capacitively coupled and distinct electromechanical resonators by leveraging this silicon nitride membrane resonator. We explore phonon-cavity electromechanics based on a simple theoretical model which is analogous to optomechanics. At room temperature, we experimentally demonstrate electromechanically

induced transparency and amplification of the input signal by controlling the electromechanical energy transfers (in the form of phonons) to create signal interferences in the coupled system. We observe mechanical anti-damping effects (with respect to the applied driving tone) in both coupled drums generated by the phonon-cavity force, exhibiting the trend expected by the theoretical model. These results indicate that this new type of device design could serve for phonon-based information processing in both classical and quantum regimes, and is potentially useful for building multifunctional compact mechanical systems.

3.1. Transparency and amplification, in a single sideband pumping scheme

As introduced in Section 2.3, transparency and amplification are created based on a two-tone drive scheme that generates destructive and constructive interference between the probe signal and the signal generated by photon cycling in optomechanical circuits. Both phenomena can be served in many coupled systems, also in coupled mechanical system. The simplest way is to make an analogy to the optomechanical system by choosing the resonator with the higher resonant frequency as the cavity, the so-called phonon cavity. The two-tone driving method is to use one signal to probe one of the coupled resonators and the other signal to pump the phonon cavity at its sideband.

In the year 2020 [71], I have achieved a silicon nitride membrane nanoelectromechanical resonator. This unique device design consists of two membrane resonators, which is advantageous for studying phonon-cavity nanoelectromechanics. As shown in figure 3.1, the device scheme is equivalent to a capacitor consisting of two movable parallel plates. Both of them have resonance frequencies in MHz range, far from each other. Therefore, we can choose a silicon nitride membrane having the $\Omega_m/(2\pi) > 8$ MHz as the phonon-cavity. Its typical bandwidth is $\gamma_c(SiN)/(2\pi) < 10^3$ Hz. In a standard microwave optomechanical circuit, the damping rate of the couple mechanical resonator γ_m is much smaller than that of microwave cavity γ_c, $\gamma_m < \gamma_c$. However, in this phonon-cavity system, the damping rate of Al membrane $\gamma_m(Al)$ is much higher than the "cavity" damping rate, with "$\gamma_m > \gamma_c$". It means the energy-leaking speed of the coupled resonator (here, Al membrane) is much faster than that of the cavity (the silicon nitride membrane).

3.1.1. Modelling of capacitively coupled two membranes

The parametric coupling between two membranes is established in this electromechanical model by leveraging the electrostatic force, which is dependent on the mechanical displacement of both resonators. This simple device structure allows to consider two parametrically coupled electromechanical resonators as a single capacitor $C_g\left(X_1, X_2\right)$ consisting of two parallel and movable membranes. The mechanical displacement of each membrane is described by $X_1(t)$ and $X_2(t)$ resonating at the frequency Ω_1 and Ω_2, with $\Omega_1 > \Omega_2$. We therefore model these two

coupled drums in the linear response regime, driven by an electrostatic force

$$F_{1,2}(t) = \frac{(V_{dc}+V_{ac})^2}{2}\frac{\partial}{\partial X_{1,2}}C_g\left(X_1, X_2\right), \tag{3.1}$$

via the following equations of motion for the displacement $X_1(t)$ and $X_2(t)$,

$$\begin{aligned}
\ddot{X}_1 + \gamma_1\dot{X}_1 + \Omega_1^2 X_1 &= \frac{V_{ac}V_{dc}}{d\,m_1}C_{g0}\left[1 - \frac{2(X_2-X_1)}{d}\right], \\
\ddot{X}_2 + \gamma_2\dot{X}_2 + \Omega_2^2 X_2 &= \frac{V_{ac}V_{dc}}{d\,m_2}C_{g0}\left[-1 + \frac{2(X_2-X_1)}{d}\right].
\end{aligned} \tag{3.2}$$

Here, the $\gamma_{1,2}$ is the mechanical damping rate, the $m_{1,2}$ is the effective mass, and C_{g0} is the initial capacitance between two membranes separated by a distance d. The driving force $F_{1,2}(t)$ is modeled as a simple parallel plate capacitor, and the force is truncated at the Taylor expansion of the $C_g(x)$, $\approx C_{g0}(1 - \frac{x}{d} + \frac{x^2}{d^2})$, with $x(t)$=$X_2(t) - X_1(t)$. In the Eq.3.2, an approximation $2V_{dc}V_{ac} + V_{ac}^2 \approx 2V_{dc}V_{ac}$ has been made by considering a general case in measurements: $V_{dc} \gg |V_{ac}|$. The static contribution V_{dc}^2 has been dropped of the equation since it cannot drive resonantly the modes; note however that this term can be employed to tune the resonance frequencies [71]. We shall not refer to this possibility in the present work.

To demonstrate phonon-cavity in a two-tone driving scheme, the membrane having the higher resonance frequency is chosen as phonon-cavity (with index 1). The other coupled mechanical resonator with the lower resonance frequency is marked with index 2. We exploit one driving tone with frequency Ω_d to weakly probe one of the coupled membranes around Ω_1 or Ω_2 and the other one with frequency Ω_p to pump the phonon-cavity at its sideband $\sim \Omega_1 \pm \Omega_2$. Therefore, we also write V_{ac} in the form of $V_{ac}(\Omega_p, \Omega_d) = \frac{\mu_p}{2}e^{-i\Omega_p t} + \frac{\mu_d}{2}e^{-i\Omega_d t} + c.c.$ The Eq.3.2 can be analytically solved in the rotating frame through looking for the displacement driven by the probe signal, $X_{1(2)}(t)$=$\frac{x_{1(2)}(t)}{2}e^{-i\Omega_d t} + c.c$ and the displacement of the other coupled membrane generated by the frequency mixing between the probe and the pump signals, $X_{2(1)}(t)$=$\frac{x_{2(1)}(t)}{2}e^{-i(\Omega_p \mp \Omega_d)t} + c.c.$ The $x_{1(2)}$ is the slowly varying complex amplitudes of mechanical displacements.

First, we drive the phonon-cavity at the frequency with small amplitude around its resonance frequency Ω_1 with the frequency detuning δ, Ω_d=Ω_1+δ. (a) Pump the photon-cavity at its red sideband with the frequency Δ detuned from Ω_1-Ω_2, Ω_p=Ω_1-Ω_2+Δ. Based on an approximation that $\Omega_1^2 - \Omega_d^2 \approx 2\Omega_1(\Omega_1 - \Omega_d)$, the analytical solution of Eq.3.2 gives

$$\begin{aligned}
x_1 &= \frac{f_d}{2m_1\Omega_1}\frac{1}{\frac{1}{\chi_1} - \frac{|f_p|^2\chi_2}{4m_1m_2d^2\Omega_1\Omega_2}}, \\
x_2 &= -\frac{f_p^*}{2m_2\Omega_2}\frac{x_1}{d}\chi_2
\end{aligned} \tag{3.3}$$

(b) For pumping the photon-cavity at its blue sideband at the frequency Ω_p=Ω_1+Ω_2+Δ, it

arrives

$$
\begin{aligned}
x_1 &= \frac{f_d}{2m_1\Omega_1}\frac{1}{\frac{1}{\chi_1}+\frac{|f_p|^2\chi_2}{4m_1m_2d^2\Omega_1\Omega_2}},\\
x_2^* &= \frac{f_p^*}{2m_2\Omega_2}\frac{x_1}{d}\chi_2
\end{aligned}
\tag{3.4}
$$

Here, we define the susceptibility of the phonon-cavity χ_1 and the mechanical susceptibility χ_2 corresponding to both red and blue sideband pumping the phonon-cavity.

$$
\begin{aligned}
\chi_1 &= \frac{1}{-\delta - i\frac{\gamma_1}{2}},\\
\chi_2 &= \frac{1}{\Delta - \delta - i\frac{\gamma_2}{2}},
\end{aligned}
\tag{3.5}
$$

The $f_p = \frac{C_{g0}V_{dc}\mu_p}{d}$ and $f_d = \frac{C_{g0}V_{dc}\mu_d}{d}$ are complex amplitudes respectively corresponding to the pumping and driving force. To have analogues of optomechanical system, we define the coupling strength as $G = \frac{\partial\Omega_1}{\partial X_2} \approx \frac{\partial\Omega_1}{\partial C_g}\frac{\partial C_g}{\partial X_2} \approx\text{-}\frac{\Omega_1}{2d}$. It gives single phonon coupling strength g_0=$G\sqrt{\frac{\hbar}{2m_2\Omega_2}}$, where $\sqrt{\frac{\hbar}{2m_2\Omega_2}}$ is the zero-point fluctuations of the coupled membrane with resonance frequency Ω_2. Therefore, the term of $\frac{|f_p|^2}{4m_1m_2d^2\Omega_1\Omega_2}$ can be re-written as $n_pg_0^2$ through making a definition of the phonon number $n_p \approx \frac{2|f_p|^2}{m_1\Omega_1^2}\frac{1}{\hbar\Omega_p}$, generated by the pump tone. Then, Eq.3.4 becomes:

$$
x_1 = \frac{f_d}{2m_1\Omega_1}\frac{1}{\chi_1^{-1} \pm n_pg_0^2\chi_2},
\tag{3.6}
$$

where "-" and "+" symbols correspond to "red" and "blue" sideband pumping scheme.

Second, we probe the coupled membrane at the frequency around its resonance frequency Ω_2 with the frequency detuning δ, Ω_d=Ω_2+δ. Similarly, an approximation of $\Omega_2^2 - \Omega_d^2 \approx 2\Omega_2(\Omega_2 - \Omega_d)$ has been made. For pumping the photon-cavity at its red sideband, the analytical solution of Eq.3.2 gives

$$
\begin{aligned}
x_2 &= -\frac{f_d}{2m_2\Omega_2}\frac{1}{\chi_2^{-1} - n_pg_0^2\chi_1},\\
x_1 &= -\frac{f_p^*}{2m_1\Omega_1}\frac{x_2}{d}\chi_1,\\
\chi_1 &= \frac{1}{-\Delta - \delta - i\frac{\gamma_1}{2}},\\
\chi_2 &= \frac{1}{-\delta - i\frac{\gamma_2}{2}}.
\end{aligned}
\tag{3.7}
$$

For the blue sideband pumping, it arrives

$$\begin{aligned} x_2 &= -\frac{f_d}{2m_2\Omega_2}\frac{1}{\chi_2^{-1} - n_p g_0^2 \chi_1^*}, \\ x_1^* &= -\frac{f_p^*}{2m_1\Omega_1}\frac{x_2}{d}\chi_1^*, \\ \chi_1^* &= \frac{1}{\delta - \Delta + i\frac{\gamma_1}{2}}, \\ \chi_2 &= \frac{1}{-\delta - i\frac{\gamma_2}{2}}. \end{aligned} \tag{3.8}$$

3.1.2. Analytical calculation for single-tone sideband pumping scheme: analogy to optomechanical damping effect

The two parallel membranes can be likened to the two coupled movable mirrors in optomechanics. Thus, it is interesting to verify the "phonon-cavity" forces back-action effects on both membranes. Here, we define the phonon-cavity is sideband pumped at $\Omega_p = \Omega_1 + \beta$, where β is the frequency detuning from the resonance frequency of the phonon-cavity Ω_1. The mechanical displacement of the coupled membrane (with the index 2) is written as $x_2(t) = \frac{1}{2}\delta x_2(t)e^{-i\Omega_2 t} + c.c$, where the complex amplitude of $\delta x_2(t)$ is the Brownian motion of the the membrane(2) [36]. The terms where motion $x_2(t)$ multiplies pump amplitude in Eq.3.2 generate harmonics at $\Omega_n = \Omega_p + n\Omega_2$, with n $\in \mathbb{Z}$. The solution can be found in the form of the *ansatz*,

$$x(t) = \sum_{n=-\infty}^{+\infty} \frac{\delta x(t)}{2} e^{-i(\Omega_p + n\Omega_2)t} + c.c. \tag{3.9}$$

In this work, we are interested only in schemes of $n = \pm 1$, corresponding to the "down" and "up" sideband of the pump signals at the frequency $\Omega_- = \Omega_p - \Omega_2$ and $\Omega_+ = \Omega_p + \Omega_2$. The solution of the phonon-cavity motion equation in Eq.3.2 is given by

$$\begin{aligned} x_- &= \frac{e^{-i\Omega_- t}}{2}\frac{f_p \delta x_2^*}{m_1 d}\frac{1}{\Omega_1^2 - \Omega_-^2 - i\Omega_-\gamma_1} + c.c, \\ x_+ &= \frac{e^{-i\Omega_+ t}}{2}\frac{f_p \delta x_2}{m_1 d}\frac{1}{\Omega_1^2 - \Omega_+^2 - i\Omega_+\gamma_1} + c.c. \end{aligned} \tag{3.10}$$

It yields an extra force, $f_{cav} = \frac{f_p}{d}x_-^* + \frac{f_p^*}{d}x_+ + c.c$, biasing on the membrane(2), which modifies the initial mechanical susceptibility to become

$$\begin{aligned} \chi_2(\Omega) &= \frac{1}{2m_2\Omega_2}\frac{1}{(-\Omega - i\frac{\gamma_2}{2}) + \Sigma}, \\ \Sigma &= \frac{|f_p|^2}{4m_1 m_2 d^2 \Omega_1 \Omega_2}\left(\frac{\Omega_2 + \beta - i\frac{\gamma_1}{2}}{(\Omega_2 + \beta)^2 + \frac{\gamma_1^2}{4}} - \frac{\Omega_2 - \beta - i\frac{\gamma_1}{2}}{(\Omega_2 - \beta)^2 + \frac{\gamma_1^2}{4}}\right) \end{aligned} \tag{3.11}$$

The imaginary part of Σ modifies the mechanical damping rate γ_2, yielding additional damping γ_{opt}

$$\gamma_{opt} = n_p g_0^2 \left[\frac{\gamma_1}{(\Omega_2 + \beta)^2 + \frac{\gamma_1^2}{4}} - \frac{\gamma_1}{(\Omega_2 - \beta)^2 + \frac{\gamma_1^2}{4}} \right]. \tag{3.12}$$

The real part of Σ contributes to a frequency shift of Ω_2,

$$\delta\Omega_2 = -n_p g_0^2 \left[\frac{\beta + \Omega_2}{(\Omega_2 + \beta)^2 + \frac{\gamma_1^2}{4}} - \frac{\Omega_2 - \beta}{(\Omega_2 - \beta)^2 + \frac{\gamma_1^2}{4}} \right]. \tag{3.13}$$

Both expressions of Eq.3.12 and Eq.3.13 refer to "optical damping effect" and "optical spring effect" in optomechanics. The f_{cav} corresponds to the phonon-cavity force, originating from energy confined in the capacitor that consistsof two capacitively coupled membranes.
Using same method, we could get the dynamical backaction effects on the phonon-cavity,

$$\begin{aligned} \gamma_{opt(cavity)} &= n_p g_0^2 \left[\frac{\gamma_2}{(\Omega_2 - 2\Omega_1 - \beta)^2 + \frac{\gamma_2^2}{4}} - \frac{\gamma_2}{(\Omega_2 - \beta)^2 + \frac{\gamma_2^2}{4}} \right], \\ \delta\Omega_1 &= n_p g_0^2 \left[\frac{\Omega_2 - 2\Omega_1 - \beta}{(\Omega_2 - 2\Omega_1 - \beta)^2 + \frac{\gamma_2^2}{4}} + \frac{\Omega_2 - \beta}{(\Omega_2 - \beta)^2 + \frac{\gamma_2^2}{4}} \right]. \end{aligned} \tag{3.14}$$

3.1.3. Two-tone measurement results of the coupled membranes

In order to build the interference process, one of the key points is that the unprobed mechanical resonator should provide enough phonons to be fed back by the pump tone, generating interference with the initial probe tone. In addition, these two coupled electromechanical resonators can be driven and read out separately, we can thus probe one of the resonators without damaging the excitation states of the phonon-cavity. Energies, in the form of phonons, can be coherently cycled between both systems.

Figure 3.2 shows two-tone measurement results of the coupled silicon nitride membrane and Al membrane, at room temperature. In a red sideband pumping scheme, (a) electromechanical response of the phonon-cavity measured with driving amplitudes $V_{dc} = 4$ V, $V_{ac}(\Omega_d) = 1$ mV$_p$, $V_{ac}(\Omega_p) = 70$ mV$_p$, and probed at $\Omega_d = \Omega_1 + \delta$; (b) mechanical response of the Al drum measured with driving amplitudes $V_{dc} = 2$ V, $V_{ac}(\Omega_d) = 3$ mV$_p$, $V_{ac}(\Omega_p) = 100$ mV$_p$, and probed at $\Omega_d = \Omega_2 + \delta$. In a blue sideband pumping scheme, (c) the phonon-cavity response obtained with driving amplitudes $V_{dc} = 4$ V, $V_{ac}(\Omega_d) = 0.7$ mV$_p$, $V_{ac}(\Omega_p) = 70$ mV$_p$, and probed at $\Omega_d = \Omega_1 + \delta$; (d) simultaneously measured the corresponding spectra at the frequency $\Omega_p - \Omega_d$. The Δ is the frequency detuning regarding the pump tone, with Ω_p=$\Omega_1 \pm \Omega_2$+Δ for a red or blue sideband pumping scheme. (e)-(h) Simulation results for the measurements shown in (a)-(d), which were performed by using the theoretical model described in Eq.3.3, Eq.3.4, Eq.3.7, Eq.3.8. All experimental parameters are mentioned above. The measurement results can be qualitatively fitted well by using our model.

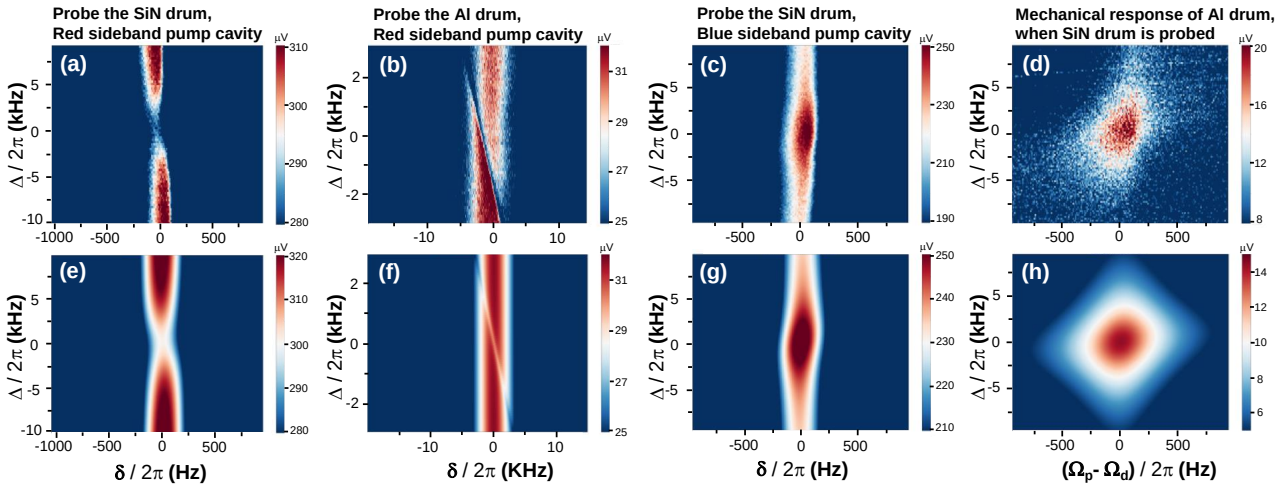

Figure 3.2: Electromehanically induced transparency and amplification in two capacitively coupled membranes. On the top, measurement results; the bottom: calculation results.

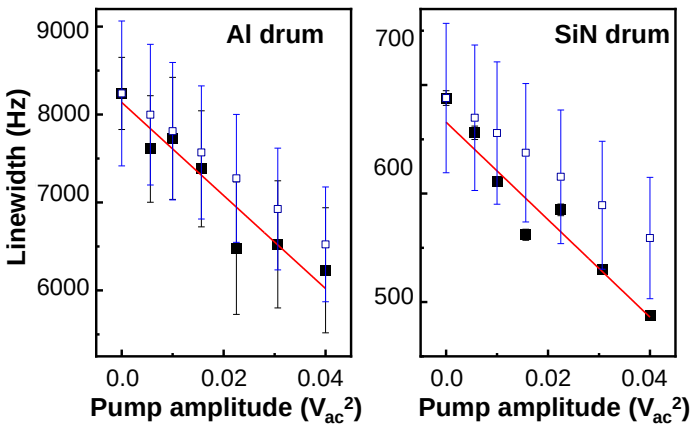

Figure 3.3: In a blue sideband pumping scheme $\Omega_p = \Omega_1 + \Omega_2$, the linewidth of the Al drum and the SiN drum.

For standard microwave optomechanical circuits, the cavity is fabricated on the chip and cannot be in a vibration state. It is therefore not possible to observe the cavity forces affecting the other side of the "microwave mirror", in analogy to optical systems. Compared to microwave optomechanical circuits, the phonon-cavity system offers more flexibility in understanding how the "cavity forces" affect two parallel and movable "mirrors".

Figure 3.3 shows measurement results of linewidth of both Al and silicon nitride membrane, which are decreasing as a function of the *ac* pump power $[V_{ac}^2(\Omega_p)]$, as shown in black squares. The dc bias is $V_{dc} = 4\text{V}$, the probing voltage $V_{ac}(\Omega_d) \approx 500\ \mu V$ for the Al drum and the probing voltage $V_{ac}(\Omega_d) \approx 200\ \mu V$ for the SiN drum. Red lines are linear fits of the data. The white squares with blue edges are calculation results based on our model and experimental parameters mentioned above. There is a small offset between the measurement and calculation results, which could be induced by inaccuracy in the device parameters, e.g. d, m_1, and m_2. We can see that the pump tone adds energy from external to this coupled system and makes anti-damping effects on both movable subjects. Because both resonators are coupled through the same electrostatic force.

3.2. Multi-tone driving: Squeezing mechanical motion in multi-mode coupling

As discussed earlier, in an optomechanical scheme, single-sideband pumping of the cavity will produce optical damping effects in a single-tone driving scheme, because of the back-action effects. Then, double pump operation offers a method to cancel the back-action effects from the pump tone. It is called back-action evading measurements, in standard optomechanical system. This method offers measurements with sensitivities that exceed the standard quantum limit, and potentially allows for the generation of quantum squeezed states [72]. In our phonon-cavity nanoelectromechanical system, we also can perform such an operation to squeeze signal with more degrees of freedom compared with standard 2ω parametric pumping [27]. We therefore rewrite the basic equations of motion of two membranes as Eq.3.15

$$\begin{aligned}
\ddot{X}_1 + \gamma_1 \dot{X}_1 + \Omega_1^2(1+p_1)X_1 &= \eta_1 \left[1 - \frac{2(X_2 - X_1)}{d}\right] (\sum_i^{+\infty} V_i[\omega_i] + V_{dc})^2, \\
\ddot{X}_2 + \gamma_2 \dot{X}_2 + \Omega_2^2(1+p_2)X_2 &= \eta_2 \left[-1 + \frac{2(X_2 - X_1)}{d}\right] (\sum_i^{+\infty} V_i[\omega_i] + V_{dc})^2,
\end{aligned} \tag{3.15}$$

by considering multi-tone driving and the parametric modifications of the spring constant in each nanomechanical resonator. The $X(t)_{1,2}$ is the mechanical displacement, with frequency around resonance frequency $\Omega_{1,2}$. The $\gamma_{1,2}$ is the mechanical damping rate of the membrane. The $p_{1,2} = \delta\kappa_{1,2}/\kappa_{1,2}$ indicates the modulations of spring constant $\kappa_{1,2}$. The $\eta_{1,2} = C_g/(d\, m_{1,2})$ is the device parameter, determined by the effective mass $m_{1,2}$ of the membrane '1' and '2' and the capacitance C_g between two membranes which are separated with an initial distance d. In this work, we focus on investigations of double pump effects in a phonon-cavity nanoelectromechanical system. We thus keep only i = r, d, b, which we rename in 'r' (red), and 'b' (blue)

sideband pump tone, and 'd' for the driving tone, respectively. The electrostatic force acting on both membranes are created through combinations of a dc signal V_{dc} and the high frequency signals, with an amplitude V_i carrying the angular frequency ω_i. The three-tone operation is designed to use two pump tones to pump the resonator with the higher resonance frequency in this coupled system at its red and blue sidebands, respectively. At the same time, one of the resonators is probed by the third tone around its resonance frequency. The signal for the red pump tone is written as $V_r[\omega_r] = \frac{1}{2}\mu_r e^{-(i\omega_r t+\varphi_r)} + c.c$, with μ_r the complex amplitude of the red pump tone and the frequency $\omega_r = \Omega_1 - \Omega_2$. The same definition of $V_b[\omega_b]$ is applied for the blue pump tone with the frequency $\omega_b = \Omega_1 + \Omega_2$ and the phase φ_r. The mechanical displacement $X(t)_{1,2}$ is written as $X(t)_{1,2} = \frac{x_{1,2}}{2}e^{-i\omega t+\epsilon}$ + c.c with $x_{1,2}$ the complex amplitude of motion translated in frequency around the resonance frequency of the membrane $\Omega_{1,2}$. For the probe tone, we first consider the third tone $V_d[\omega_d] = \frac{1}{2}\mu_d e^{-(i\omega_d t+\epsilon)} + c.c$, to probe at the aluminum membrane's resonance frequency, $\omega_d = \Omega_2$.

The basic method of solving this kind of coupled motion equation is to first find the solution of the un-probed motions, here the X_1,

$$-i\Omega_1\gamma_1\,\frac{x_1}{2} + \frac{1}{2}\,p_1\,\Omega_1^2(\frac{1}{2}e^{-i\phi_r-i\phi_b}\,\mu_r\,\mu_b)x_1^* = -\frac{2\,\eta_1}{d}V_{dc}(\frac{1}{2}e^{-i\phi_r}\,\mu_r x_2 + \frac{1}{2}e^{-i\phi_b}\,\mu_b x_2^*). \tag{3.16}$$

The second term in the Eq.3.16 comes from the frequency mixing of the two pump tones (the blue and the red pump), which contributes to the parametric modification of the diaphragm spring constant. The most interesting thing is that the parametric modulations have a phase-dependent characteristic. On the right-hand side of the Eq.3.16, both terms play role of driving forces. One may notice that the mixing terms between the one of the pump tone and the driving tone (e.g $\mu_r\mu_d$, $\mu_b\mu_d^*$) will also generate driving forces, acting on X_1. Considering the experimental settings, $V_{dc} \gg \mu_d$, these terms can be therefore neglected. They result from the electrostatic coupling, as a function of the mechanical displacement of membrane X_2.

$$-i\Omega_2\gamma_2\,\frac{x_2}{2} + \frac{1}{2}\,p_2\,\Omega_2^2(\frac{1}{2}e^{i\phi_r-i\phi_b}\,\mu_r^*\,\mu_b)x_2^* = -\eta_2\,e^{-i\epsilon}\,V_{dc}\,\mu_d - \frac{2\,\eta_2}{d}V_{dc}(\frac{1}{2}e^{i\phi_r}\,\mu_r^* x_1 + \frac{1}{2}e^{-i\phi_b}\,\mu_b x_1^*). \tag{3.17}$$

The same method is applied to have the the motion equation Eq.3.17.The approximation, $\mu_r\mu_b \gg \mu_d^2$, is made because the probe tone is always much smaller than the pump tone in the real experiment. Expressions of both X_1 and X_2 can be obtained by solving Eq.3.16, Eq.3.17, and their conjugate expressions. It is easy to see that the displacements of the two coupled membranes have a phase dependence characteristic, regardless of whether they are probed or not, as shown in Fig.3.4. In other words, the noise carried by both nanomechanical resonators can be squeezed by double pump tones, at the same time.

In the experiment, the 3rd tone is used to probe one of the coupled resonators, with a small amplitude in the order of a few hundred μV. If we take the probe signal as a reference, the double pump will bring a relative phase in the rotation frame. We call it the red phase ϕ_r and the blue phase ϕ_b. Figure 3.5 shows the measurement results of the probe signal around Ω_1, presenting phase-sensitive effects. In the quadrature plane, squeezing the signal in this double pump scheme is not as simple as a standard 2Ω parametric pumping in mechanical system [73].

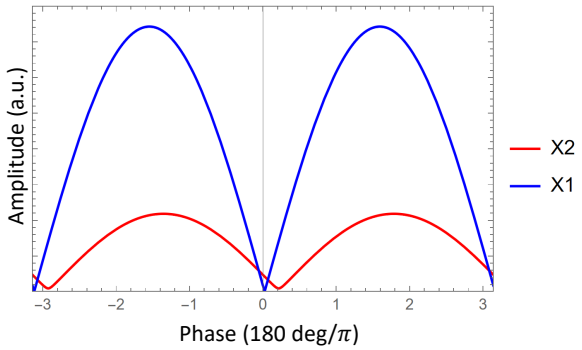

Figure 3.4: Calculation results of the X_1 and X_2 as a function of demodulation phase, when the Al mechanical resonator is probed at its resonance frequency.

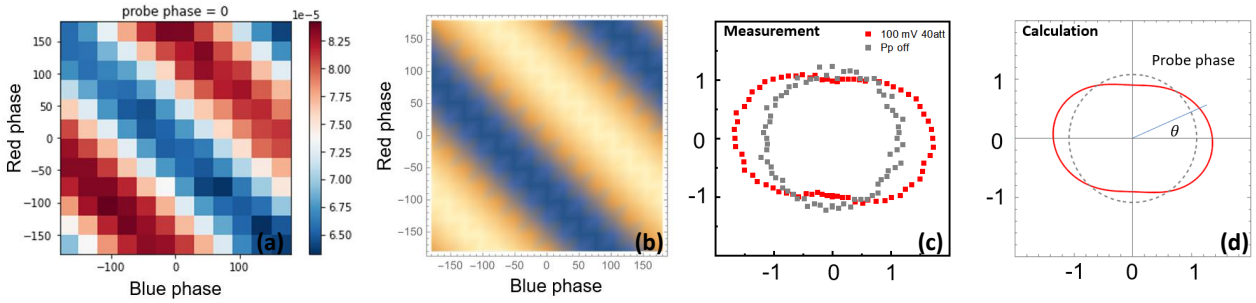

Figure 3.5: (a) probe signal amplitude, as a function of the blue pump phase and the red pump phase. (c) Parametric plots of two quadratures of the probe signal. Gray squares correspond to the pump off and red squares are measured based on the double pump scheme. Both (b) and (d) are calculation results based on Eq.3.16 and Eq.3.17.

Because two phases are deducted from each other, it looks more like two coupled rings in the quadrature plane. Such operations can be used to squeeze signals/noise or explore phase-based logic gates.

3.3. Summary of chapter 3

In contrast to traditional microwave optomechanical circuits, the phonon-cavity nanoelectromechanics offers a distinct advantage: it enables direct probing of the low-frequency resonator without compromising the energy confined within the 'cavity'. Because, in nanoelectromechanical system, the dissipation mainly come from mechanical properties. This approach not only enhances our understanding of optomechanics through investigations of coupled nanomechanical systems but also capitalizes on the rich physics of optomechanics. This richness enables coherent signal routing within the coupled system, the development of the tunable filters/amplifiers in radio frequency ranges, and the exploration of novel types of logic gates. **Importantly, these studies lay the groundwork for realizing networks of coupled oscillators in multifunctional mechanical systems**.

4. A scanning tip combined with microwave interferometry for mapping mechanical vibrations

To date, a variety of sensitive transduction schemes have been achieved for the detection and manipulation of nanomechanical resonators. These mainly include methods based on electrical detection or optical interferometry. The former technology is widely used for testing electrically integrated nanomechanical systems, which requires the design and nanofabrication of on-chip circuits to detect and control vibrating elements. However, this technique does not have the spatial resolution required to study localised mechanical vibrations. On the other hand, optical interferometry offers high sensitivity in terms of spatial resolution and direct transmission of the detected signals. Unfortunately, it is challenging to detect the resonators made of the materials with transparent or low reflectivity characteristics. Integrating optical interferometry into a cryostat for low-temperature measurements is also not straightforward. In recent years, taking advantage of the decreasing size of the vibrating elements, both probe microscopy [74, 75, 76, 77] and electron microscopy [78, 79] have also been developed. They not only facilitate the readout of these mechanical resonators with extremely small interaction volumes (such as carbon nanotubes), but also open up access to the study of local mechanical properties [78], engineering mechanical impedance [76], and hybridised nanomechanical systems [75]. However, so far, in most previous relevant works on probe microscopy, the scanning tips act as an active sensing/probing element and one relies on complex phase-locked loops, photo-detectors, or additional driving circuits on the chip. Also, for the electron microscopy, it still needs an additional force source to excite nano-vibrations of the massive element, which poses a challenge for combinations with standard electron microscopy chambers.

Scanning microwave microscopy (SMM) has demonstrated its ability to detect capacitances at the aF scale and their variations, enabling the characterisation of a wide range of materials [80, 81]. It allows us to take advantage of the high sensitivity of microwave technologies and the spatial resolution of the scanning tip. In recent years, microwave interferometry has been used to detect tiny displacements of MEMS that enables both the drive and the detection signals to be transmitted through a single gate electrode [71, 82]. These previous works inspired me to extend the SMM approach by integrating with microwave interferometry to detect and manipulate the nanomechanical vibrations of a massive resonator through a single scanning tip for the first time. Besides, SMM integrated in SEM has been achieved several years in IEMN. Unfortunately, its application is limited to the characterisation of materials, and fewer and fewer people are using it.

In this chapter, I show the ability of the SMM to spatially image nanomechanical vibration modes, without contact with the vibrating silicon nitride membrane. It enables the investiga-

tion of spatial dependencies (over the membrane size) while scanning the tip position. I will also present coherent energy transfers between the scanning tip and the membrane resonators through parametric coupling, based on phonon-cavity nanoelectromechanics [82]. Typical optomechanical features were observed in this phonon-cavity electromechanics, including "optomechanical damping effects" and electromechanically induced transparency. Our work not only extends the current applications of SMM, but also demonstrates that this system provides a novel platform for the detection of nanomechanical systems integrated into a complex circuit [29]. Furthermore, it may serve as a valuable tool for investigating phonon-phonon interactions where precise control of the interactions is required [83, 84]. Some parts of experimental results have been recently published [85].

4.1. Measurement setup

The whole setup consists of two parts. One is the setup of scanning microwave microscopy 4.1.1, used for operations of the scanning tip positions. The other part is microwave interferometry, which is exploited to drive and to read the mechanical vibrations 4.1.2. Both two parts are well separated for the operation and measurement. The more technical details of the setup can be found in the supporting information parts of our publication [85].

4.1.1. Setup of Scanning Microwave Microscopy

The experimental setup consists of an atomic force microscopy (AFM) which can work in contact mode. For this, we choose the general deflection laser approach using a fiber-coupled laser source Fabry-Perot (λ= 635 nm, 2 mW) to generate the optical beam. A feedthrough passage allows the connection of the optical fiber into the SEM chamber. After reflection on the cantilever, the optical beam is detected on a quadrant photodiode giving deflection, friction, and sum signals. A modified 25Pt300D cantilever from Rocky Mountain Nanotechnology (see at https://rmnano.com/) redesigned to support a transverse electromagnetic mode (TEM) through a propagating microstrip structure with a signal line of 300×100 µm is first mounted on the probe holder. The alignment of the laser spot on the cantilever is performed before the set-up is placed under vacuum. We tune the PSD (power spectrum density) and laser collimator positions to align the spot with the PSD center position. For the beam being focalized on the cantilever, we adjust the PSD positioners and monitor the detected signals to set the horizontal and vertical deflection values near zero and maximize the sum signal. The laser power is then set to 2 mW.

In this measurement setup, we exploit a metallic tip as a suspended and movable top gate, which is soldered onto a 50 Ω impedance PCB. The nanoelectromechanical resonator, measured in this work, is a silicon nitride circular membrane, ≈ 90 nm in thickness and $a \approx 16$ μm in radius, as shown in Fig.4.1(b). The fabrication process of this silicon nitride membrane has been reported in [71]. The sample is fixed on the nano-positioner with X-Y-Z relative displacements up to a nanometer precision. The tip is glued on a printed circuit board (PCB) and the membrane is grounded through bonding wires. During the measurement, the membrane is held in a vacuum

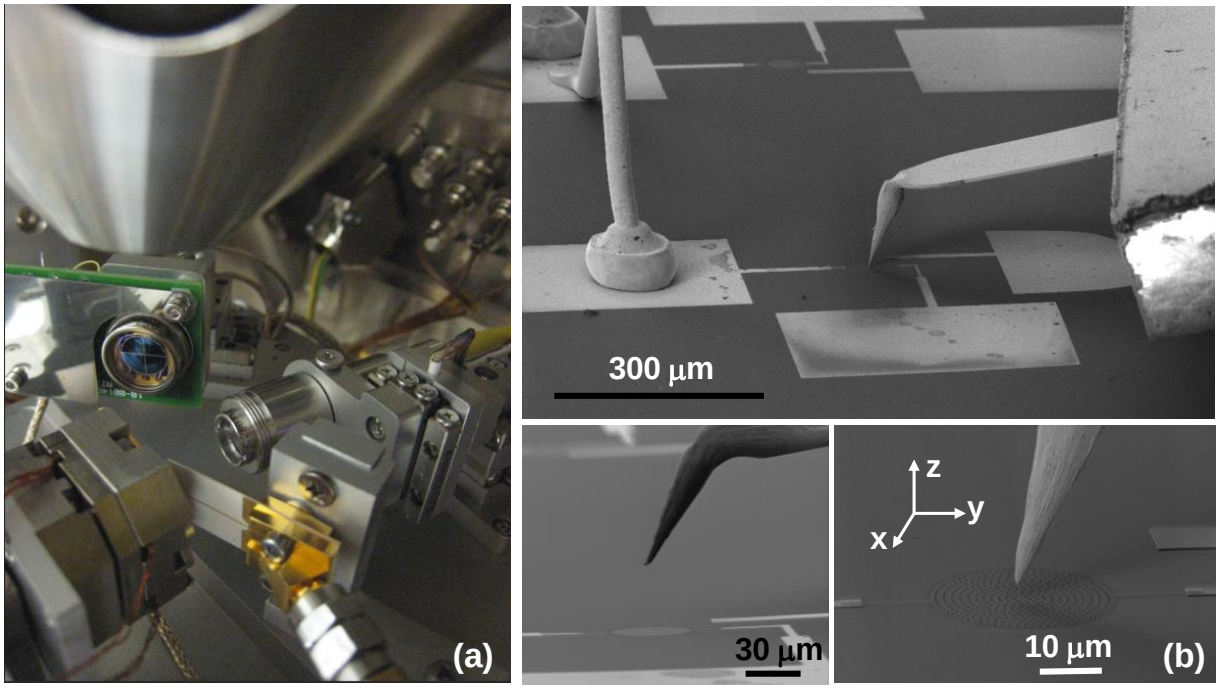

Figure 4.1: (a) Photo image of setup inside the vacuum chamber, (b) SEM image of a metallic tip suspended on the top of the silicon nitride circular membrane.

chamber (below $\sim 5 \times 10^{-4}$ mbar) at room temperature. A scanning electron microscope (SEM) has also been installed in this vacuum chamber. Figure 4.1 (b) shows SEM images of the scanning tip and the membranes. The tip is not perpendicular to the sample surface and forms a small angle with the Z axis.

4.1.2. High-frequency setup for driving and reading out of mechanical motions

The high-frequency setup consists of two parts, as shown in Fig.4.2. The first part is the generation of electrostatic forces to excite mechanical motion, which is generated by combining V_{dc} and V_{ac} signals through a bias tee. The second part is the readout scheme where we use microwave interferometry. The microwave signal of the frequency ω, analogous to a laser beam, is shone directly onto the mechanical resonator. Due to non-linearity, the reflected microwave signal carries the mechanical signal at frequency $\omega + \Omega_m$. A microwave circulator is used to separate the reflected microwave signal from the input probe signal. This reflected signal is read by frequency down-conversion using a microwave mixer, followed by a Zurich Instrument locking amplifier (UHFLI). A single port on the tip combines both drive and readout signals. All the high-frequency setup for driving and reading the mechanical movements is kept in the atmosphere.

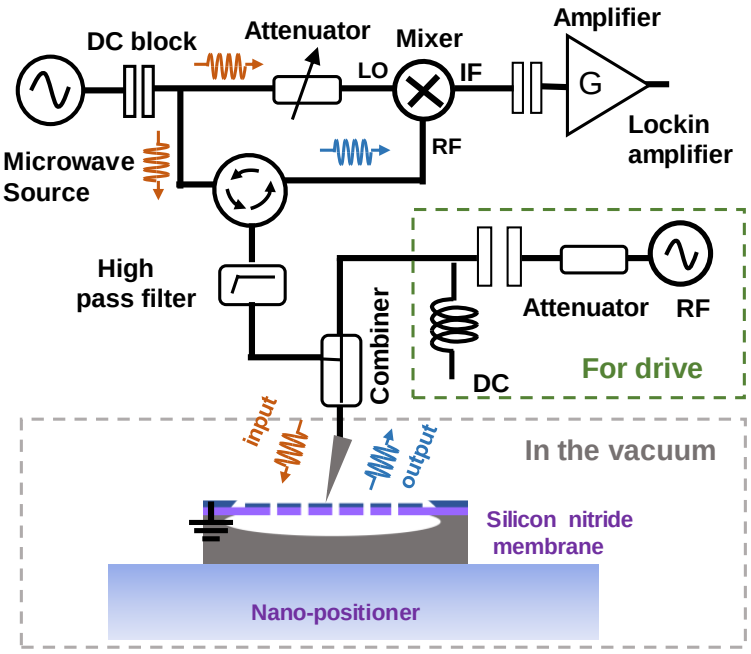

Figure 4.2: Schematic diagram of the high frequency electrical set-up for both driving and detection of the chip.

4.2. Image the mode shape

The spatial mode shape of a circular membrane, $\psi_{m,n}(r,\phi)$, is described by

$$\psi_{m,n}(r,\phi) = A_0 \cdot Cos(m\phi) \cdot J_m(\frac{\alpha_{m,n} r}{a}), \tag{4.1}$$

with m and n respectively denoting the azimuth and radial mode number. The r and ϕ are the polar coordinates, and $\alpha_{m,n}$ is determined from the solutions of the n-th Bessel function of the first kind $J_m(\alpha_{m,n}) = 0$ under the condition $r = a$ [86]. The A_0 is a normalization value chosen such that the $\psi_{m,n}$=1, where the motion is maximum. Its eigenfrequency $\Omega_{m,n}$ thus can be identified from the value of the ratio $\Omega_{m,n}/\Omega_{0,1}$, which follows the corresponding ratio of $\alpha_{m,n}/\alpha_{0,1}$ [71].

The procedure of mapping mechanical mode shapes begins with positioning the tip relative to the membrane. The SEM is employed to help the alignment of the tip and the membrane, as shown in Fig. 4.1. After calibrations of the tip position, the tip is then positioned on top of the membrane at a fixed height H. To excite mechanical vibrations, an electrostatic force F is generated between the tip and the coupled membrane at the frequency Ω_d, $F = \frac{\partial C_g(\mu)}{\partial \mu} V_{dc} V_{ac} \cdot Cos(\Omega_d t)$, though the combination of a dc voltage V_{dc} and a ac signal $V_{ac} \cdot Cos(\Omega_d t)$. Here, μ is the mechanical displacement. The readout of the mechanical motion relies on the microwave interferometry [71]. A microwave signal at the frequency $\omega/2\pi = 6$ GHz

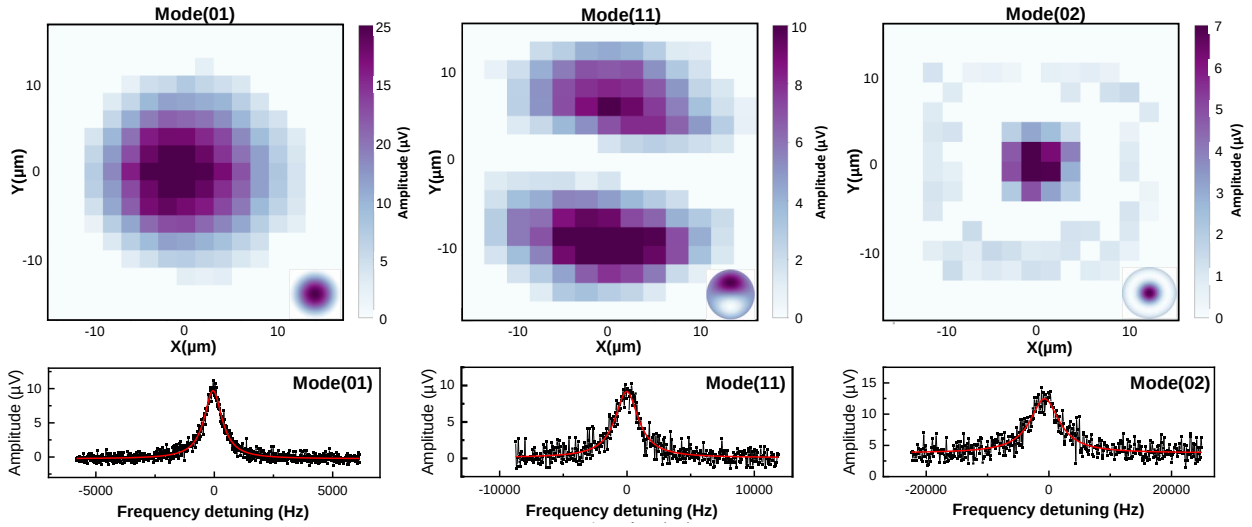

Figure 4.3: Top: measured amplitude of the resonance peaks as a function of spatial position (X-Y), corresponding to each vibration mode $\Omega_{0,1}/(2\pi) \approx 8.82$ MHz, $\Omega_{1,1}/(2\pi) \approx 14.06$ MHz, and $\Omega_{0,2}/(2\pi) \approx 20.25$ MHz. Inset, the calculation results of the expected modes, based on Eq.4.1. Bottom: mechanical response of the silicon nitride membrane, measured at the location in the X-Y plane corresponding to the maximum signal amplitude.

is directly shined to the membrane through the same tip. The reflected signal at the frequency $\omega + \Omega_d$ is then read out by a lock-in amplifier after frequency down-conversion. Three resonance frequencies have been detected. Their correspondence mechanical modes can be easily identified from the ratio of these resonance frequencies. See the method described in Eq.4.1. The resonance frequency gradually drifted towards a relatively lower frequency each time the SEM was switched on and off. It could be induced by the deposition of amorphous carbon due to the organic residues in the SEM chamber [87]. After a few months of measurement, the first mode drifts a few hundred kHz.

To map the vibration mode, we sweep the tip position in the X-Y plane with a step of 2 μm while exciting the membrane's vibration with constant external *ac* and *dc* signals. The spatial mode maps depicting the vibrations of the circular membrane are generated by plotting the amplitude of the detected signal at the resonance frequency as a function of the tip position in the X-Y plane, as shown in Fig. 4.3. These measurement results reflect the relative vibration amplitudes of the nanomechanical membrane, as the amplitude of the detected electrical signal is directly proportional to the mechanical vibration amplitude [71]. Compared with the vibration of a circular membrane based on Eq. 4.1, these measurement results reveal a minor spatial asymmetry. This is due to the imperfect alignment between the tip and the Z-axis of the chip.

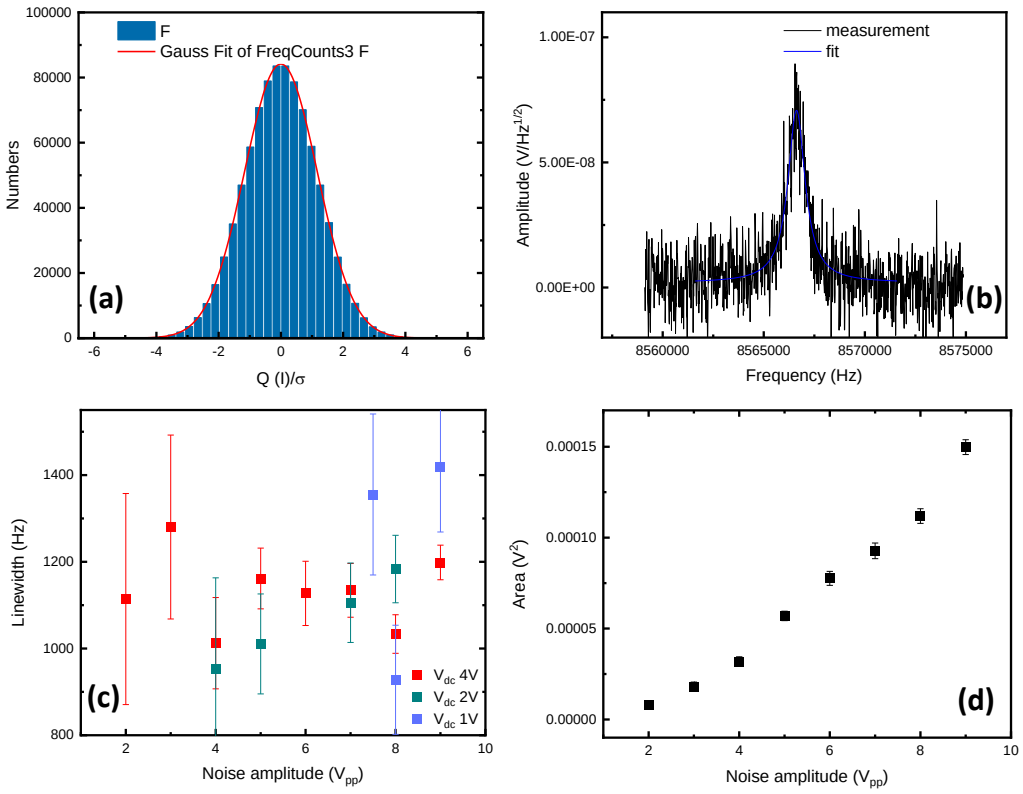

Figure 4.4: Top: (a) White noise amplitude I and Q, (b) Spectrum of membrane resonator, excited by external white noise, (c) Linewidth of membrane resonator as a function of noise amplitude, corresponding to different DC bias, (d) Area versus input white noise amplitude V_{pp}. Each area is obtained by integrating the measurement results of the noise spectrum density, e.g. the data shown in the (b).

4.3. Artificial heating of the silicon nitride membrane by stochastic forces through the scanning tip

Here is a demonstration of artificial heating of the membrane through the tip. To do so, a noise source is connected to the tip through a home-made band pass filter. The white noise is filtered around the resonant frequency of the membrane. We then verify whether the noise is white noise. The statistics of both quadratures of the noise amplitude were measured and are presented as Gaussian distributions, as shown in Figure 4.4 (a). Figure 4.4 (b) shows a spectral density of the membrane that is excited by the stochastic forces. In other words, the input white noise artificially heats up the membrane resonator. The temperature of the mode increases as the amplitude of the noise increases because the integrated area of the spectral density increases. It has been observed that the linewidth of the nanomechanical resonator displays random variations. It may be due low-frequency noise-induced self-heating of the tip itself.

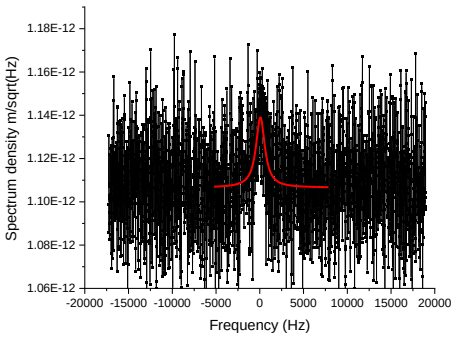

Figure 4.5: Spectral density of membrane's displacements, measured by exciting the membrane through external stochastic forces.

Besides, in order to test the sensitivity of this tip detection scheme, we also tried to add the minimal white noise to the tip in order to have the thermal Brownian motion of the membrane just above the noise floor of the detection chain, as shown in Fig.4.5. The detected noise floor is around 1.12 pm/$\sqrt{Hz}$ and the detected peak is 20 fm/$\sqrt{Hz}$ out of the noise floor. Note that the measured spectrum density presents the same detection sensitivity that we obtained from two coupled membrane resonators (without tip) [88]. The conversion between the detected amplitude (v) and the vibration (m) is based on the microwave interferometry methods (see Section5.1.2, Eq.5.3). The transduction factor in this SMM measurement is 1.2 $\times 10^{11} V^2/m^2$, the same order of the optical interferometer used in the detection of graphene nanodrums ($3.75 \times 10^{11} V^2/m^2$) [89].

4.4. Parametrical coupling between the tip and the membrane

As described above, the tip is capacitively coupled to the membrane. Therefore, by modulating the capacitance between two spatially separated mechanical modes, a parametric coupling can be created. It allows to coherently manipulate energy transfer between two modes, here, the tip mode and the membrane mode. Here, we probe the membrane and pump its blue sideband at the frequency $\Omega_{tip} + \Omega_m$. Thus it is a two-tone measurement. The basic principle has been described in section 3.1.1. Figure 4.6 (a) shows a mechanical response of the membrane, when it is blue sideband pump. Because the γ_{tip} is smaller than that of the membrane, its mechanical responses are projected within the bandwidth of the membrane's resonance. In this blue sideband pumping scheme, the linewidth of the tip is $\gamma_{tip}/(2\pi) = 15$ Hz, which is smaller than the initial linewidth when there is no pump tone. The pump tone generates the phonon cavity force acting on the tip by modulating its susceptibility, and further the linewidth. The blue pump tone reduces the line width of the tip, known in optomechanics as the anti-damping effect. It may therefore provide an opportunity to improve the sensitivity of a conventional scanning tip

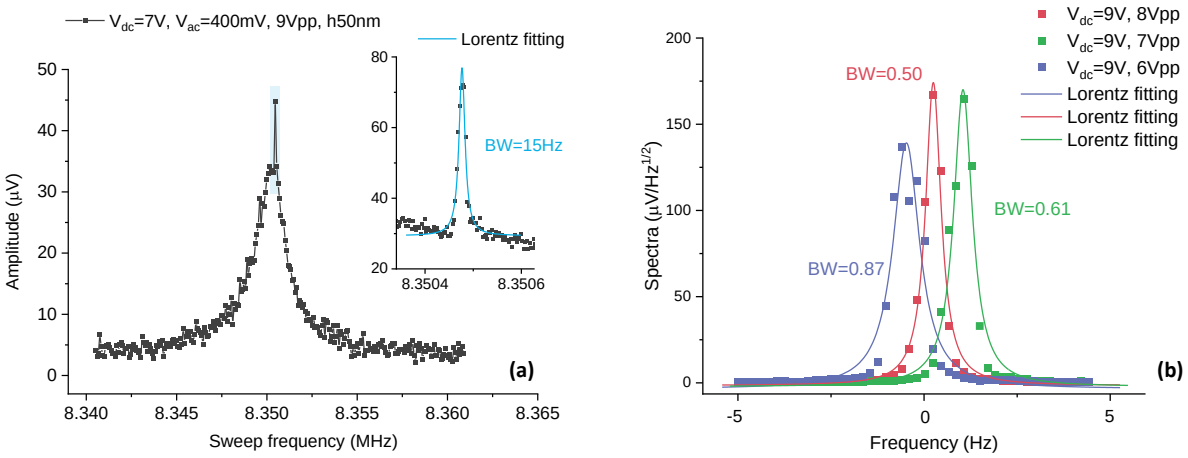

Figure 4.6: Left: mechanical responses of the membrane resonator, when it is blue sideband pumped. The illustration is a zoomed-in measurement of the tip response. Right: spectra density, detected around the Ω_m.

by taking advantage of the blue sideband pumping technique.

In comparison to the double drum coupling (see chapter 3), it is easier to observe the thermal Brownian motion spectrum density of the tip in this tip-drum coupled system. Because the tip is clamped at a single side and its spring constant is quite small, $\sim$ 18 N/m (https://www.rmnano.com/technical-data and https://www.rmnano.com/substrates). Thus, we use a single tone, no probe tone, to pump the membrane at its blue sideband to amplify the initial thermal Brownian motions. As shown in Fig. 4.6(b), the linewidth is quite small, $\gamma_{tip}/(2\pi) < 1$ Hz. The frequency responses exhibit unstable states (self-oscillations), the frequency randomly shifting and the amplitude randomly beating.

4.5. Mechancial damping, induced by detection scheme

The scanning tip gives spatial resolution in imaging of the mechanical damping. Figure 4.7 (a) shows V_{dc} dependence of the mechanical linewidth, measured in the centre of the membrane with $V_{ac} = 30$ mV$_p$, with H = 300 nm for the square with black and white colors, H = 400 nm for the white dots. We see a monotonous increase with V_{dc}. Here, the H is the distance between the tip and the surface of the coupled membrane. It is clear that the linewidth corresponding to V_{dc} around 1 V is about 50 % of the value measured with $V_{dc} > 7$ V. Besides, the linewidth also presents a tip-height dependence, as shown in Fig.4.7 (b). It gives the impression that mechanical damping is tuned by the external electrostatic forces. However, it is quite different from previous reports that damping exhibited a quadratic behavior [90, 78].

Here, we develop a capacitive circuit damping model to understand this phenomenon. We

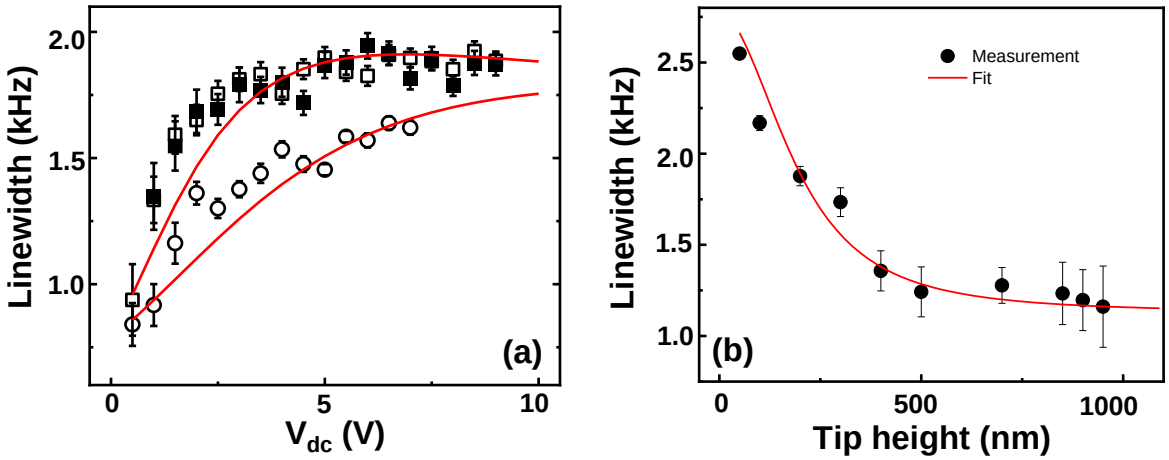

Figure 4.7: (a) The linewidth of the fundamental mode of the membrane, as a function of V_{dc}. (b) Linewidth of the membrane as a function of the tip height, measured at V_{dc} = 5 V and V_{ac} = 30 mV_p. Fit results are shown as solid red lines.

define the current passing in the Al/silicon nitride layer to be

$$\begin{aligned} I &= \mathrm{d}Q_c/\mathrm{d}t \\ &\approx (V \cdot \mathrm{d}C_g/\mathrm{d}x)(\mathrm{d}x/\mathrm{d}t) + C_g \mathrm{d}V/\mathrm{d}t. \end{aligned} \tag{4.2}$$

The first term corresponds to the displacement current and the second term comes from the capacitance current. Considering the definition of mechanical displacement $\mu(t) = \mu_0 \cdot Sin(\Omega_m t)$ and V $= V_{dc} + V_{ac} \cdot Sin(\Omega_m t)$, the expression of the current passing through resonator is given by $I \approx (V_{dc} + V_{ac})\frac{C_{g0}}{H}\mu_0\Omega_m \cdot Cos(\Omega_m t) + C_{g0}\Omega_m V_{ac} \cdot Cos(\Omega_m t)$, in the condition of the $V_{dc} \gg V_{ac}$ and with the approximation that $\partial C_g/\partial\mu \approx C_{g0}/H$. The C_{g0} and H are the coupling capacitance between the tip and the coupled membrane, and the distance between them respectively. Therefore, the energy dissipated per period by the displacement current becomes

$$\begin{aligned} E_{dis} &\approx R\int_0^{2\pi/\Omega_m} I^2 \mathrm{d}t, \\ \int_0^{2\pi/\Omega_m} I^2 \mathrm{d}t &= (\frac{V_{dc}^2\mu_0}{H} + 2V_{ac}V_{dc})\pi\Omega_m C_{g0}^2\frac{\mu_0}{H}. \end{aligned} \tag{4.3}$$

The total kinetic energy stored in the resonator E_k is given by $E_k = \frac{1}{2}m_{eff} \cdot \Omega_m^2 \cdot \mu_0^2$, where m_{eff} is the effective mass of the vibrating element. Considering the definition of quality factor,

$$\begin{aligned} Q &= 2\pi E_k/E_{dis} \\ &= m_{eff}\Omega_m H^2/(RV^2C_{g0}^2). \end{aligned} \tag{4.4}$$

The total damping of the nanomechanical system γ_m arrives

$$\gamma_m \approx \gamma_0 + \frac{(V_{dc}^2 + 2V_{ac}V_{dc}\frac{H}{\mu_0})C_{g0}^2}{m_{eff}H^2} \cdot R. \tag{4.5}$$

Now, we analyze the resistance resulting dissipation in the equivalent RLC circuit model for the capacitive drive and detection scheme. In the well-known analogy, the mechanical resistance $R_m = \gamma_0 m_{eff}/(V_{dc}\partial C_g/\partial\mu)^2$ [91, 92]. Considering the fabrication process of the membrane resonator, the high-resistive silicon substrate may contribute to a parallel circuit with the membrane suspended on its top. This can be caused by the thin layer of aluminium deposited on the membrane reaching the part of the silicon substrate through these holes. We therefore assume the existence of a resistive element with conductance σ_0, parallel to R_m in the device scheme. It gives the total equivalent resistance R

$$\begin{aligned} R &= \frac{1}{\sigma_0(1+\epsilon\cdot V_{dc}^2)}, \\ \epsilon &= \frac{1}{m_{eff}\cdot\gamma_0\cdot\sigma_0}(\frac{\partial C_g}{\partial\mu})^2 \end{aligned}. \tag{4.6}$$

The measurement results of the linewidth as a function of V_{dc} and as a function of tip height, shown in Fig.4.7, can be well fit by this analytical model, based on the Eq.4.5.

4.6. Summary of chapter-4

A novel platform based on scanning microwave microscopy has been integrated with microwave interferometry. The scanning tip, which acts as a suspended top gate, is used to drive and detect the tiny displacements of a nanomechanical resonator without the need for physical contact with the sample. The scanning tip, with its features of spatial resolution, has demonstrated its unique ability to image the mechanical vibration mode and to investigate the linear damping properties in the membrane. In addition, manipulations of energy coherently transferred in two spatially separated mechanical modes have been demonstrated in this parametrically coupled tip-membrane system. This novel platform not only extends the current applications of SMM to the MEMS/NEMS domain but also provides a unique opportunity to study electromechanical properties at the nanoscale, in particular to conveniently study these vibrating elements embedded in a complex circuit, such as microwave optomechanical circuits [29]. For instance, in standard microwave optomechanical circuits, the nanoelectromechanical resonator is integrated with LC superconducting circuits and cannot directly connect to external circuits for testing. But, with this SMM technology, it is feasible to in-situ characterize the mechanical properties. Besides, the concept of this experimental configuration will further facilitate research activities to go beyond the current frontiers of quantum sensing and quantum engineering. For example, it can be used to study a few numbers of phonon tunneling and non-reciprocal phonon transfer across vacuum through quantum fluctuations [83, 84], by taking advantage of microwave readout schemes which feature high sensitivity and low heating effects. In addition, it also gives access to study Casimir effects and thermal dynamics in both classical and quantum regimes.

It is difficult to compare this scanning microwave microscopy technique with other developed scanning tip techniques, such as the atomic force microscopes (AFM), scanning tunneling microscope (STM), or laser interferometry. Regarding the resolution and noise level, this scanning microwave microscopy cannot reach the current state of the art in imaging vibration modes.

This microwave scanning probe technique relies on electrostatic interactions between the tip and its coupled membrane. It is therefore necessary to have a relatively large tip size and a small distance between the tip and the membrane, to obtain sufficient detectable signals. Then it has no advantage over AFM and laser interferometry in terms of high spatial resolution. The key aspect here is that microwave techniques are directly compatible with quantum electronics, and especially the toolbox developed for microwave optomechanics. Besides, microwave photons are much less energetic than optical photons and suit much better cryogenic environments. In this respect, the developed technology here beats qualitatively all others (STM, AFM) which cannot compete on that level.

5. Experimental setups and development of silicon nitride membrane electromechanical resonators

The experimental setups have been designed to characterize microwave optomechanical devices and nanoelectromechanical resonators, in a capacitive coupling scheme. Because capacitive transducers are extremely sensitive and can act as passive vibration elements in their coupled systems. The setup work consists of circuit design, wiring measurement chains, sample holder fabrications, programming control codes, and so on. Three measurement schemes have been developed for microwave optomechanical devices: 2D superconducting microwave cavity coupled with NEMS (for low temperature measurement only), microwave optomechanical hybrid circuit, and 3D microwave cavity coupled with NEMS.

After arriving at IEMN, I also started to consider a novel device design to develop an electromechanical resonator with excellent mechanical properties at room temperature while ensuring effective coupling with external circuits. It is also desirable for microwave optomechanical circuits (see discussions in 2.1.5). Because the coupling rate between the silicon nitride doubly-clamped beam and the microwave cavity is quite low [29]. Based on fruitful discussions on the fabrication process with the Litho team in IEMN, silicon nitride membrane nanoelectromechanical resonators have been achieved. The unique feature enables the exploration of multi-modes in microwave optomechanical circuits and phonon-cavity electromechanical functions with a large coupling rate. These building blocks are essential for the pursuit of neuron-inspired computing functions using NEMS networks.

5.1. Setup: integration of microwave optomechanics and microwave interferometry

So far, I have developed several measurement setups for measuring microwave optomechanical devices and electromechanical resonators, at various temperature ranges, from 2D to 3D microwave cavities. All these designs are based on the mechanical resonator being capacitively coupled to external circuits or similar devices. The reason for choosing a capacitive coupling scheme is that it offers high sensitivities and its integrated circuit can be passive with low dissipation. All readout method in my work relies on microwave technologies, in the frequency range between 1 GHz to 12 GHz.

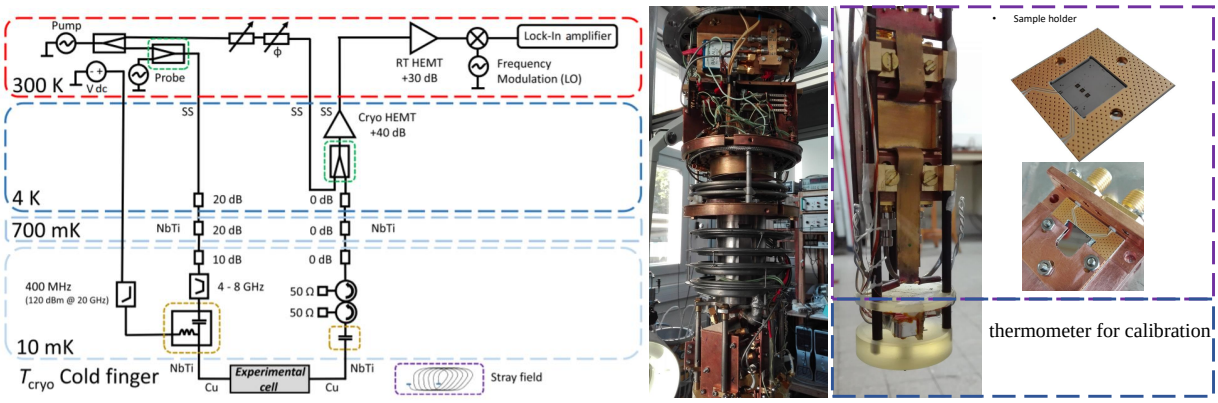

Figure 5.1: Simplified common wiring of the experimental platforms; the different levels within the demagnetization cryostat are shown with their respective temperature. SS stands for stainless steel, NbTi for niobium titanium, and Cu for Copper coaxial cables (50-Ohms impedance). The boxed elements are added and removed depending on the experimental run.

5.1.1. Low temperature microwave optomechanical platform

The first microwave optomechanical setup is for ultra-low temperature measurement, which I have developed in the institute NEEL (UBT group) 2016, Grenoble, with Eddy Collin. Figure 5.1 shows both a simplified schematic diagram of wiring the nuclear adiabatic demagnetization cryostat and setup photos [29]. They are built around a cryogenic HEMT placed at about 4 K and two circulators mounted on the mixing chamber of the dilution units. On the nuclear adiabatic demagnetization cryostat, it is a Caltech 1–12 GHz bandwidth with a measured noise of about 15 K (50 photons at 6 GHz). The (dashed-green) boxed component below the HEMT in Fig. 5.1 represents a power combiner used to realize an opposition line. The cryogenic HEMT is linear enough so this protection is not necessary. This choice is made because of space constraints: feeding an extra microwave opposition line in the nuclear adiabatic demagnetization cryostat is very demanding. The filtering of the injection lines (*dc* and microwave) is also described in Fig.5.1. The key point for building this kind of setup is to pay attention to give enough thermal contacts to the samples and avoid thermal decoupling and extra signal losses in both driving and detection chains. Each line and component has been calibrated in several cooling down and arming up cycles, although running such kind adiabatic demagnetization cryostat is extremely painful. *Thanks R. R. Gazizulin for help in running this crazy cryostat !* Until now, this setup is still in service for many experiments in Neel. With this setup, the NEEL group has successfully achieved passive cooling of a mechanical resonator to its quantum ground state using a microwave optomechanical readout scheme [93].

The sample, mounted on this setup is designed to be a single transmission line coupled with a superconducting microwave cavity through a coupling capacitor, as described in Fig.2.2(a). Thus, the setup adapts to the measurement of microwave signal in the form of transmission.

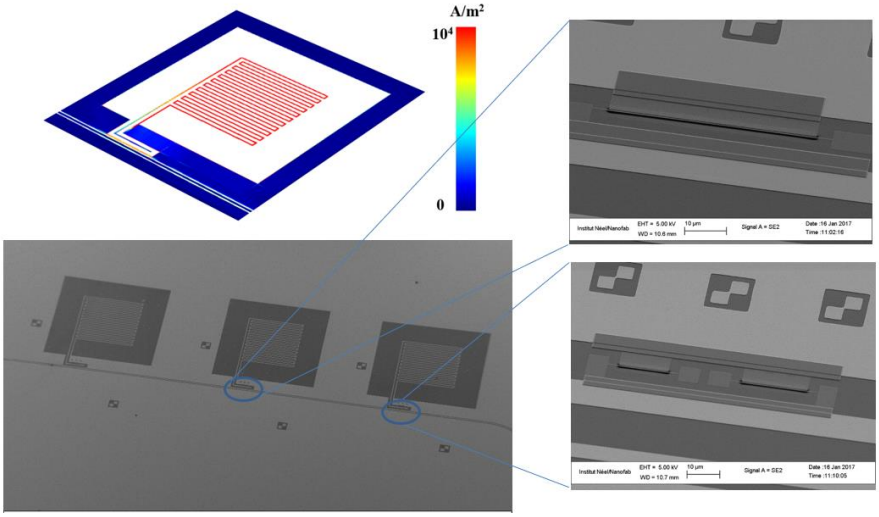

Figure 5.2: Top-left: Sonnect simulation results of a microwave resonator with lumped element design. The rest are SEM images of the fabricated superconducting microwave cavity coupled with doubly-clamped beam nanomechanical resonators.

Figure 5.2 shows SEM images of a typical microwave optomechanical circuit. The microwave cavities are realized through laser lithography and reactive ion etching of a 120 nm thick layer of niobium (Nb). The NEMS mechanical element we use as an on-chip thermometer is made from 80-nm-thick high-stress silicon nitride (SiN, 0.9 GPa), grown on top of silicon. It is a 50 μm long doubly clamped beam of width 300 nm. It is covered by a 30-nm layer of aluminum (Al), capacitively coupled to the cavity through a 100 nm gap. The aluminum part is patterned using standard e-beam lithography and lift-off, while the beam is released through RIE etching of the silicon nitride followed by a selective XeF_2 silicon etching. The silicon nitride is not removed below the niobium layer.

To achieve the desired cavity forces and photon numbers, a large Q_c is necessary (see Eq.2.36). As a result, the NEMS has been designed to be effectively isolated from external circuits. It is therefore difficult to drive/probe mechanical resonators with rf signals. It is only reachable by microwave signals in the form of microwave photons through the cavity forces. Besides, it only works at low temperatures below the transition temperature of Nb thin film, serving for quantum circuits.

5.1.2. Setup for measuring nanomechanical resonators and microwave optomechanical hybrid circuit, in a wide temperature range

To explore the practical application of optomechanical devices, I developed a second setup that integrates the microwave optomechanical scheme with microwave interferometry [71]. The microwave cavity is built based on a microstrip line with $\lambda/4$ wavelength on PCB, capacitively coupled to two parallel microstrip lines, as shown in Fig.5.4 (a) and (b). Its quality factor is

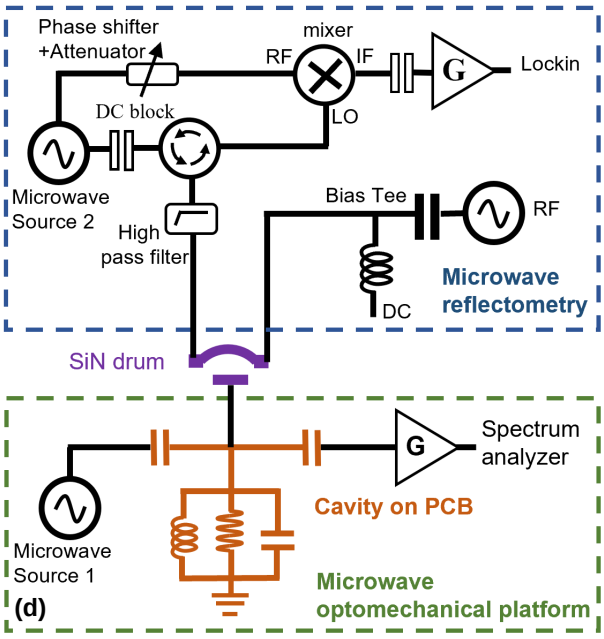

Figure 5.3: schematic diagram of measurement setup, in which the microwave cavity on the PCB part is marked in caramel color. The microwave cavity makes capacitive coupling with silicon nitride drum (purple color) via bonding wires connecting to its suspended top-gate. The SiN drum, covered with Al thin film, connects to two microstrip transmission lines through bonding wires. One is for driving the mechanical resonator and the other one is for detecting mechanical motion through a microwave reflection scheme.

obtained through standard transmission measurement. The whole design work is performed based on COMSOL multiphysics. At the resonance frequency, the electric field inside the cavity reaches the maximum value in the terminal part of the center microstrip line, as shown in Fig. 5.4 (a). The nanomechanical resonator is fabricated on a silicon chip with 50 Ohm impedance pads to prevent additional losses from microwave signals. It is then connected to the terminal part of the center microstrip line through bonding wires. This design allows for flexibility in changing samples. **However, this flexibility comes at the cost of lower quality factor values and poor confinement of the electromagnetic field inside the cavity**. The simulation result, shown in Fig.5.4 (b), presents a high-quality factor c. However, the cavity always suffers from high-frequency losses from the printed circuit board (PCB) layer, impedance mismatch from the chip, and heating effects. The quality factor measured in the experiments is around 100. The decision to create the microwave cavity on a PCB was inspired by the work of Eva Weig's group, now at TUM in Germany.

The microwave interferometry is integrated with the microwave optomechanical scheme, shown in Fig. 5.3. It is well adapted to the readout of the capacitively coupled NEMS/MEMS. To better understand how it works, an electrical circuit model is made for analysis.

The mechanical resonator can be treated as a movable capacitor $C_m(x)$, which connects a stray

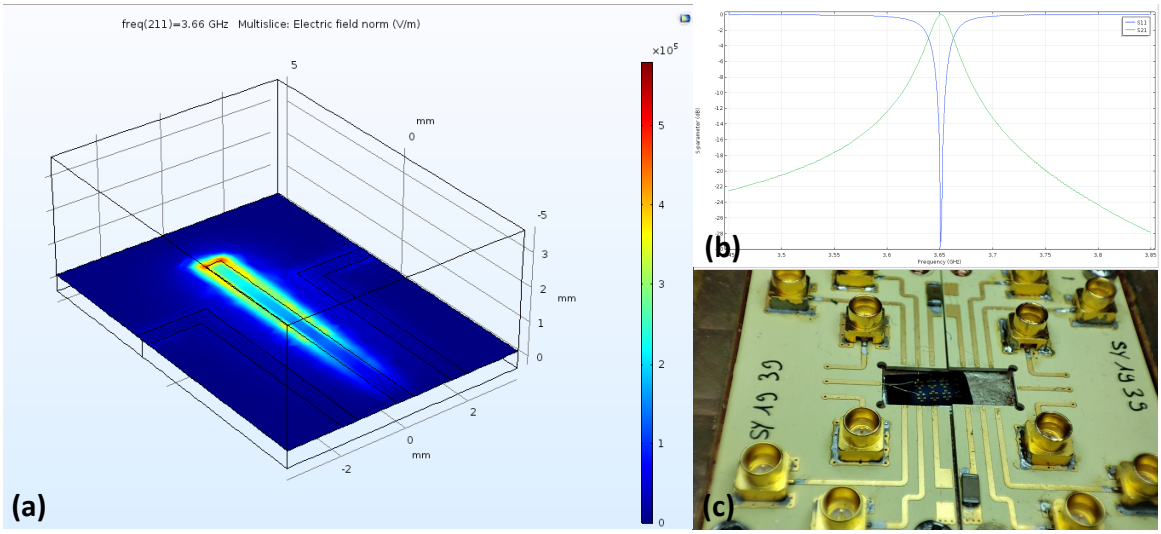

Figure 5.4: (a) COMSOL multiphysics simulation of a microstrip line with $\lambda/4$ wavelength on PCB. (b) Simulation results of S11 and S21. (C) Photo image of PCB bonded with a NEMS chip.

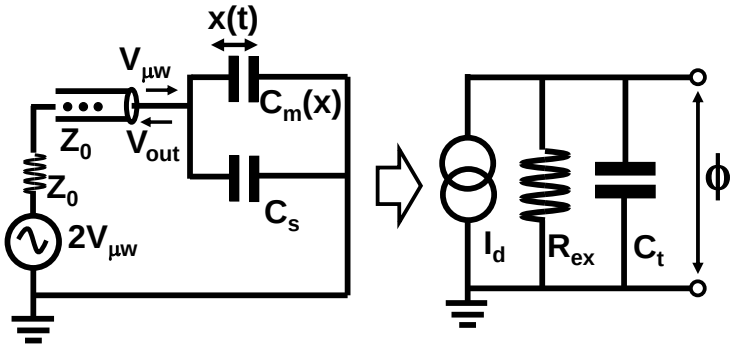

Figure 5.5: Left, the equivalent circuit of reflectometry. The $Z_0 = 50$ Ohm is the impedance of the detection part and $V_{\mu w}$ is the microwave amplitude with frequency ω delivered to the mechanical resonator. Right, its equivalent parallel RC circuit.

capacitor C_s induced by electrode pads. From Norton's theorem, it can be transferred to a parallel circuit, as shown in Fig.5.5, where the total capacitance $C_t = C_s + C_m(x)$ and equivalent resistance $R_{ex} = 1/(\omega^2 C_t^2 Z_0)$. As the $C_m(x)$ is a function of the mechanical displacement $x(t)$, we rewrite it as $C_t = C_{t0}$-$C_m x(t)/d$ where C_{t0} is the total static capacitance and d is the initial distance between the drum resonator and its coupling gate. It can be described by a motion equation of the flux ϕ biased on the $C_m(x)$,

$$(C_{t0} - \frac{C_m x}{d})\frac{\partial^2 \phi}{\partial t^2} - \frac{C_m}{d}\frac{\partial x}{\partial t}\frac{\partial \phi}{\partial t} + \frac{1}{R_x}\frac{\partial \phi}{\partial t} = I_d, \tag{5.1}$$

where $I_d = i\omega C_t V_{\mu w}$, which can be written in form of $I_d(t) = \frac{1}{2} I e^{-i\omega t} + \text{c.c.}$. Here, the I is the complex amplitude of the current. The mechanical displacement is written as $x(t) = \frac{1}{2} A(t) e^{-i\Omega_m t} + \text{c.c.}$ with A the (complex) amplitude translated in frequency around the mechanical resonance frequency Ω_m. We can thus find an exact solution using the *ansatz*:

$$\phi(t) = \sum_{n=-\infty}^{+\infty} \phi_n(t) = \sum_{n=-\infty}^{+\infty} \frac{1}{2}\mu_n(t) e^{-i(\omega + n\Omega_m)t} + \text{c.c.} \tag{5.2}$$

We look for the solution V_{out} corresponding to the frequency $\omega + \Omega_m$, which was measured in the experiment. By solving motion equation 5.1 and considering input-output theory [36], the output signal is given by

$$V_{out} = \omega Z_0 \frac{C_m}{d}\frac{|x|}{2} V_{\mu w}. \tag{5.3}$$

Here, we take several reasonable approximations, $\omega/(\omega + \Omega_m) \sim 1$ and $\omega C_{t0} Z_0 \ll 1$. This is because the $\omega \gg \Omega_m$ and typical stray capacitance of C_s is in pF range. Based on Eq.5.3, we can obtain the mechanical displacement of x through this microwave reflectometry scheme. In the setup, we use the ac signal generated by the Lockin to excite the mechanical displacement $x(t)$ and probe it through a microwave signal $V_{\mu w}$ with power of 10 dBm and frequency $\omega = 4.8$ GHz. As explained above, it generates a reflected signal around V_{out}. For the measurement, we convert the V_{out} to a low frequency signal around Ω_m by demodulating it with a signal ω through a frequency mixer.

5.1.3. Setup for 3D-cavity optomechanical hybrid circuits, in a wide temperature range

Optomechanics is not limited to quantum regimes. However, to date, most microwave optomechanical cavity experimental platforms require cryogenic temperatures. Its applications are mainly limited by the quality factor of the microwave cavity as most microwave optomechanical circuits are made of superconducting materials, having very low quality factor at the temperature higher than the transition temperature of superconductivity. Although we have developed the cavity on PCB, the low-quality factor ($Q_c \sim 100$) requires a higher working power for optomechanical operations. Therefore, we are considering developing a 3D cavity platform to explore optomechanical devices over a wide working temperature range. The 3D cavity design allows electromagnetic fields to be well confined within the cavity, suppressing

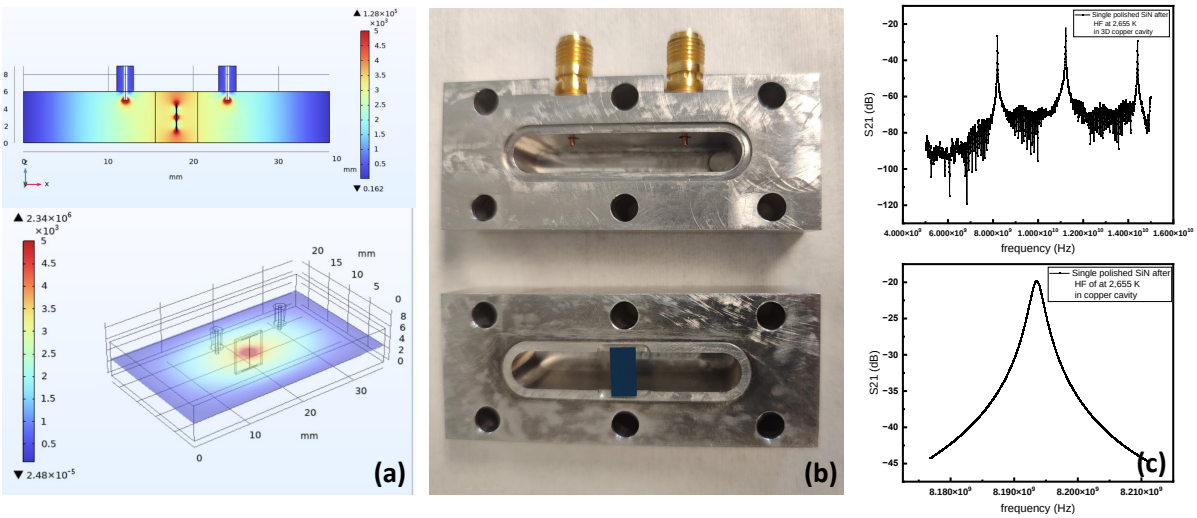

Figure 5.6: (a)Simulation results of electromagnetic field in 3D microwave cavity, for the TE_{00} mode. (b) Photo image of 3D Al microwave cavity with a silicon nitride chip. (c) Low-temperature measurement results of 3D cavity inserted with a chip. Three modes have been observed.

the effects of surface losses for microwave signals [94].

The COMSOL multiphysics is exploited to design the 3D cavity using standard SMA connectors as the emission antenna. As shown in the figure.5.6(a), the coupled chip is placed at the centre of the cavity to capture the transverse electric (TE) mode. On the chip, the coupled nanomechanical resonators will be connected to two on-chip antennas to couple with the TE_{00} mode. The chip embedded in the cavity always induces extra damping losses that decrease the quality factor, especially for coupling silicon nitride devices. In the experiment, the best Q_c obtained from silicon nitride wafers is around Q_c ~3000 at 4K. The other alternative solution is to use the bonding-chip technique to couple the silicon nitride membrane to electrodes fabricated on the sapphire substrates. So far, we are still optimizing the device design in order to adapt the 3D cavity scheme.

5.2. Development of silicon nitride membrane nanomechanical resonators

Silicon nitride strings and membranes, fabricated from pre-stressed thin films, have emerged as promising devices [95, 96]. They have nanogram (ng) effective mass m_{eff} and easily achieve MHz range resonance frequency with a high quality factor Q [97], as the pre-stress is well known for diluting the dissipation [96, 98]. Silicon nitride based micro- and nano-electromechanical systems allow electrical signals to couple with a mechanical degree of freedom and give access to electrical integration on-chip. They are of interest for both fundamental science and applications, from room temperature to mK temperature. Because of those unique proper-

ties mentioned above, Silicon nitride nano-electromechanical resonators have been exploited through their coupling to a microwave cavity, implementing an electric analog of optomechanics [1, 36].

However, the insulating feature greatly limits implementations of silicon nitride mechanical resonators in electrical systems, because a purely dielectric actuation and detection scheme is particularly weak. Up to now, composite silicon nitride doubly-clamped beams are one of the simplest and widely used device structures, in which the suspended beam is covered with a thin metal layer to generate the capacitive coupling with a side-gate. Ameliorations of coupling capacitance, for a beam structure, are normally achieved by increasing its length through lowering the resonance frequency (Ω_m) or using a demanding technique to reduce the vacuum gap [99]. Non-metallized silicon nitride beams, driven by dielectric force, provide an alternative electrical integration scheme with a high Q feature $\sim 10^5$ at room temperature [100]. Unfortunately, its typical coupling factor is quite low in microwave optomechanical platforms $\sim$ 70 Hz/nm [18]. Therefore this MEMS/NEMS conception based on a doubly clamped beam structure leaves limited space for making trade-offs among the coupling strength, Ω_m and Q_m.

For this reason, silicon nitride membranes with the specificity of a high surface-to-volume ratio motivate researchers to explore electrical integration, because they can have strong coupling with the surrounding electrical circuits. For silicon nitride based nanomechanical resonators, if we are to bridge the gap between fundamental research and the electronics industry, it is essential to explore new device designs that allow scalable architectures, integration of multiple devices, and well-controlled capacitive coupling. Thus, there is a strong motivation to explore new types of membrane resonators, with large electrical coupling effects and good mechanical properties at room and low temperature.

Between 2019 and 2020, I have developed a two-coupled membrane nanoelectromechanical system alone in clean-room, as shown in Fig.3.1. The system comprises a silicon nitride membrane capacitively coupled to an aluminium drumhead resonator. It provides access to explore a room-temperature electromechanical system that mimics a phonon-cavity, similar to optomechanics. Additionally, it allows for a silicon nitride membrane that is well-coupled with external electrical circuits, with a coupling rate increased by at least 10 times [71]. The whole process is inspired by the reflow process used in the fabrication of the air-bridge for superconducting circuits [101].

Figure 5.7 (a)-(g) shows the fabrication process of silicon nitride drum nanoelectromechanical resonators. We define the diameter of the drum by using electron beam (EB) resist CSAR62 to pattern circularly symmetric holes. The drum is released from the Si substrate by reactive ion etching (RIE) of the silicon nitride layer (SF_6: Ar = 10 sccm : 10 sccm, for 6.5 min) through these opened holes, followed by a selective XeF_2 silicon etching. These holes occupy about 40 % $\sim$ 45 % of the SiN drum area. For XeF_2 etching process, the selection rate between silicon nitride and the silicon is around $\sim$1/100. Its suspended top-gate is fabricated by using EB resist PMMA as a top-gate support through soft-bake at the temperature of 140 ^{0}C and reflowed at 170 ^{0}C. Then, we deposit the second layer EB resist MMA (methyl methacrylate) and the third layer diluted CSAR resist on the top of the support resist and pattern the gate structure. This

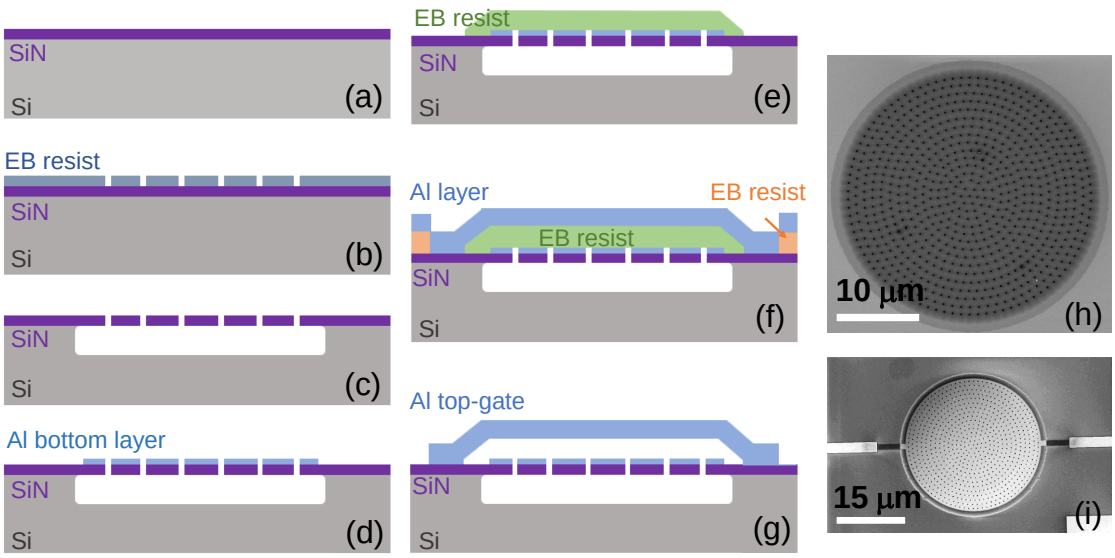

Figure 5.7: (a-g) Schema of fabrication processes. (a) starting from silicon nitride/Si wafer, (b) pattern holes for etching process (c) release silicon nitride (SiN) from Si substrate, (d) deposit Al thin film (e) pattern EB resist as a support (f) pattern top-gate and deposited Al metal (g) final device structure. (h) SEM image of the suspended silicon nitride drum, (i) SEM image of the bottom Al/silicon nitride drum

special process requires the development of a CSAR resist followed by the development of the MMA layer. For the metal depositions, we first perform Ar ion etching process to clean the sample and then use electron beam evaporation to deposit the thin films. All bonding pads on the chip are designed to be 50 Ohm impedance for microwave signals. The SEM image of the final device is shown in Fig.3.1.

In studies of silicon nitride beams and membrane resonators, it's widely acknowledged that higher tensile stress can lead to increased Q, attributed to the enhanced stored energy resulting from the stress [96, 102]. As previously discussed, the quality factor of a vibrating membrane is contingent upon both device dimensions and the tensile stress of the material. Hence, to ensure a reasonable comparison, we opted to reference results reported in the literature for a silicon nitride membrane with similar dimensions and tensile stress. In our investigation, we observed that the quality factor of a high-stress drum covered with a 25 nm Al thin film (with a diameter of 20 μm) reaches approximately 2.4×10^4 at room temperature. This value aligns closely with that of a bare silicon nitride drum detected by optical interferometry [103]. Notably, our ultra-clean nanofabrication process enables silicon nitride circular membrane to exhibit capacitive coupling without introducing additional dissipation to the device.

Besides, to verify whether the plate or membrane model is suitable for our drums, we evaluate the ratio between the tension in the drum and its bending rigidity, $\sigma 2\pi hR/(D_r/R)$, where $\sigma 2\pi hR$ is the tension with the drum and $D_r = \frac{E_r h^3}{12(1-v^2)}$ is the flexural rigidity in the plane of

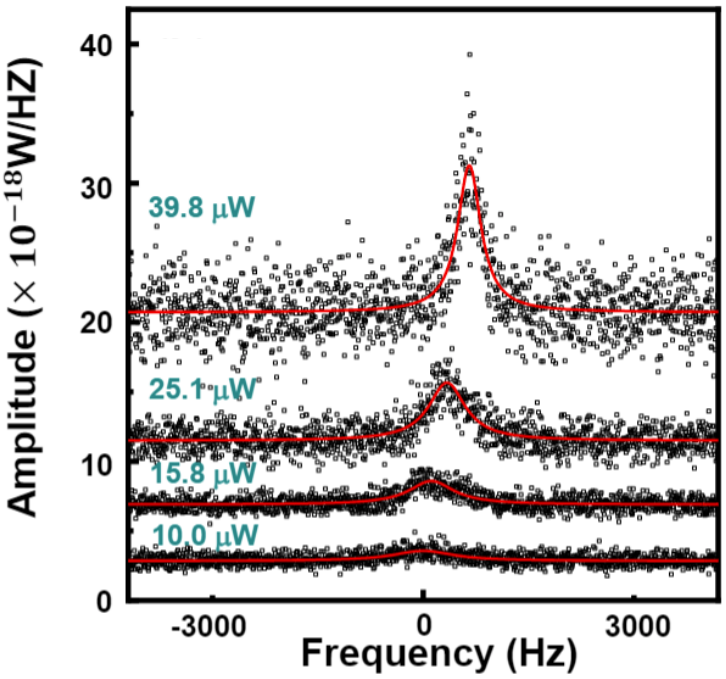

Figure 5.8: Brownian spectrum of the first mode (01) measured on the Stokes peaks, corresponding to different pump powers.

the drum, v is the Poisson's ratio, h is the thickness of the film, $E_r$is Young's modulus, and R is the radius of the drum [104, 105]. For the silicon nitride drum, by using parameters of $\sigma \sim$ in the range from 0.8 GPa to 1.0 GPa, $R = 18$ μm, $h = 80$ nm, v ~0.3, $E_r = 240$ GPa (for silicon nitride), the value of $\sigma 2\pi hR/(D_r/R)$ will be in the range from 1.1×10^4 to 1.4×10^4, exhibiting the tension-dominant property. Therefore, silicon nitride drum follows the membrane model. While, for our Al drum, it gives $\sigma 2\pi hR/(D_r/R)$ ~26 by using device parameters of $\sigma \sim 15$ MPa [106], $R = 20$ μm, $h \sim 550$ nm, v ~0.3, and $E_r = 69$ GPa (for Al). Compared with the silicon nitride drum, this Al drum approaches to the plate model, but is still a membrane.

One of the drum resonators, fabricated with the low-stress silicon nitride membrane has been integrated with a microwave cavity on PCB (see section 5.1.2 and Fig.5.4), through bonding wires. Figure 5.8. (b) shows spectra density of the first mechanical mode Ω_{01} corresponding to different pump powers. The optical damping effect is clearly observed. Through the measurement of γ_m as a function of pump power, the optomechanical coupling rate G can be obtained, 10 times higher than that of doubly-clamped beam structure (with the same length) [71].

5.3. Summary of chapter-5

In this chapter, I have presented three microwave optomechanical readout schemes. For the experiment where the mechanical resonator is to be accessible only by microwave photons, the cavity with the high quality factor is mandatory. It is better to avoid adding the DC or rf

signals to the drive system, as shown in subsections 5.1.1 and 5.1.3. Because they will introduce extra damping for the confined microwave photons. While, the hybrid readout method, combining microwave cavity and microwave interferometry, provides access to low-frequency drive lines. It gives more degrees of freedom for manipulations. However, there is a trade-off between the flexibility from low-frequency local drive and the well-confined electromagnetic fields in the cavity.

The unique device usually acts as a unique tool. It provides enough space to explore device innovations and unexplored physics. I have been fortunate to achieve the first silicon nitride membrane nanoelectromechanical resonator using a CMOS-compatible nanofabrication process. The mechanical properties of this circular membrane resonator reach the current state of the art. With this device, silicon nitride membranes are no longer restricted to optical applications. In addition, the design of the device actually consists of the other aluminium membrane, in addition to the silicon nitride one. The whole device can be treated electrically as two movable parallel plates, forming a capacitor. So far, based on this device, we have achieved integration silicon nitride membrane in microwave optomechanical system [71], coupling of distinct nanomechanical resoantors for room temperature phonon-cavity electromechanics [82], investigations of stochastic switching by using Duffing nonlinearity [88], imaging mechanical mode by using scanning microwave tip (under review of Nano Lett 2024.), multi-tone driving coupled NEMS, and the dark mode in the coupled NEMS (Oral presentation in CMD31, not published yet in 2024).

6. Perspective: Coupled NEMS/MEMS network based physical computing and quantum sensing

This chapter refers to the unpublished research results based on the Chist-ERA NOEMIA and ANR-MORETOME projects. The contexts of this chapter are available on request from the author.

6.1. Reservoir computing

6.2. Synchronization of NEMS networks in microwave optomechanical circuits, for pursuing smart sensing

6.3. Nanomechanical resonator in microwave optomechanical scheme for quantum sensing

Bibliography

[1] M. Aspelmeyer, T. J. Kippenberg, and F. Marquardt, "Cavity optomechanics," *Reviews of Modern Physics*, vol. 86, no. 4, p. 1391, 2014.

[2] O. Arcizet, P.-F. Cohadon, T. Briant, M. Pinard, and A. Heidmann, "Radiation-pressure cooling and optomechanical instability of a micromirror," *Nature*, vol. 444, no. 7115, p. 71, 2006.

[3] F. Brennecke, S. Ritter, T. Donner, and T. Esslinger, "Cavity optomechanics with a bose-einstein condensate," *Science*, vol. 322, no. 5899, pp. 235–238, 2008.

[4] A. Schliesser, O. Arcizet, R. Rivière, G. Anetsberger, and T. J. Kippenberg, "Resolved-sideband cooling and position measurement of a micromechanical oscillator close to the heisenberg uncertainty limit," *Nature Physics*, vol. 5, no. 7, pp. 509–514, 2009.

[5] W. Yu, W. C. Jiang, Q. Lin, and T. Lu, "Cavity optomechanical spring sensing of single molecules," *Nature communications*, vol. 7, p. 12311, 2016.

[6] C. M. Caves, K. S. Thorne, R. W. Drever, V. D. Sandberg, and M. Zimmermann, "On the measurement of a weak classical force coupled to a quantum-mechanical oscillator. i. issues of principle," *Reviews of Modern Physics*, vol. 52, no. 2, p. 341, 1980.

[7] B. P. Abbott, R. Abbott, T. Abbott, M. Abernathy, F. Acernese, K. Ackley, C. Adams, T. Adams, P. Addesso, R. Adhikari, *et al.*, "Properties of the binary black hole merger gw150914," *Physical review letters*, vol. 116, no. 24, p. 241102, 2016.

[8] M. H. Devoret and R. J. Schoelkopf, "Superconducting circuits for quantum information: an outlook," *Science*, vol. 339, no. 6124, pp. 1169–1174, 2013.

[9] D. Vion, A. Aassime, A. Cottet, P. Joyez, H. Pothier, C. Urbina, D. Esteve, and M. H. Devoret, "Manipulating the quantum state of an electrical circuit," *Science*, vol. 296, no. 5569, pp. 886–889, 2002.

[10] A. Bienfait, J. Pla, Y. Kubo, M. Stern, X. Zhou, C. Lo, C. Weis, T. Schenkel, M. Thewalt, D. Vion, *et al.*, "Reaching the quantum limit of sensitivity in electron spin resonance," *Nature nanotechnology*, vol. 11, no. 3, pp. 253–257, 2016.

[11] A. Bienfait, P. Campagne-Ibarcq, A. Kiilerich, X. Zhou, S. Probst, J. Pla, T. Schenkel, D. Vion, D. Estève, J. Morton, *et al.*, "Magnetic resonance with squeezed microwaves," *Physical Review X*, vol. 7, no. 4, p. 041011, 2017.

[12] V. Schmitt, X. Zhou, K. Juliusson, B. Royer, A. Blais, P. Bertet, D. Vion, and D. Esteve, "Multiplexed readout of transmon qubits with josephson bifurcation amplifiers," *Physical Review A*, vol. 90, no. 6, p. 062333, 2014.

[13] C. Regal, J. Teufel, and K. Lehnert, "Measuring nanomechanical motion with a microwave cavity interferometer," *Nature Physics*, vol. 4, no. 7, pp. 555–560, 2008.

[14] J. D. Teufel, T. Donner, M. Castellanos-Beltran, J. W. Harlow, and K. W. Lehnert, "Nanomechanical motion measured with an imprecision below that at the standard quantum limit," *Nature nanotechnology*, vol. 4, no. 12, pp. 820–823, 2009.

[15] J. Teufel, T. Donner, D. Li, J. Harlow, M. Allman, K. Cicak, A. Sirois, J. D. Whittaker, K. Lehnert, and R. W. Simmonds, "Sideband cooling of micromechanical motion to the quantum ground state," *Nature*, vol. 475, no. 7356, p. 359, 2011.

[16] C. Ockeloen-Korppi, E. Damskägg, J.-M. Pirkkalainen, M. Asjad, A. Clerk, F. Massel, M. Woolley, and M. Sillanpää, "Stabilized entanglement of massive mechanical oscillators," *Nature*, vol. 556, no. 7702, pp. 478–482, 2018.

[17] M. Pernpeintner, T. Faust, F. Hocke, J. P. Kotthaus, E. M. Weig, H. Huebl, and R. Gross, "Circuit electromechanics with a non-metallized nanobeam," *Applied Physics Letters*, vol. 105, no. 12, p. 123106, 2014.

[18] T. Faust, P. Krenn, S. Manus, J. P. Kotthaus, and E. M. Weig, "Microwave cavity-enhanced transduction for plug and play nanomechanics at room temperature," *Nature Communications*, vol. 3, p. 728, 2012.

[19] J. S. Huber, G. Rastelli, M. J. Seitner, J. Kölbl, W. Belzig, M. I. Dykman, and E. M. Weig, "Squeezing of thermal fluctuations in a driven nanomechanical resonator," *arXiv preprint arXiv:1903.07601*, 2019.

[20] B. Yurke and J. S. Denker, "Quantum network theory," *Physical Review A*, vol. 29, no. 3, p. 1419, 1984.

[21] A. Cottet, *Implementation of a quantum bit in a superconducting circuit*. PhD thesis, PhD Thesis, Université Paris 6, 2002.

[22] M. Göppl, A. Fragner, M. Baur, R. Bianchetti, S. Filipp, J. Fink, P. Leek, G. Puebla, L. Steffen, and A. Wallraff, "Coplanar waveguide resonators for circuit quantum electrodynamics," *Journal of Applied Physics*, vol. 104, no. 11, p. 113904, 2008.

[23] A. A. Clerk, M. H. Devoret, S. M. Girvin, F. Marquardt, and R. J. Schoelkopf, "Introduction to quantum noise, measurement, and amplification," *Reviews of Modern Physics*, vol. 82, no. 2, p. 1155, 2010.

[24] C. Gardiner, P. Zoller, and P. Zoller, *Quantum noise: a handbook of Markovian and non-Markovian quantum stochastic methods with applications to quantum optics*. Springer Science & Business Media, 2004.

[25] C. Gardiner and P. Zoller, *The quantum world of ultra-cold atoms and light book ii: The physics of quantum-optical devices*, vol. 4. World Scientific Publishing Company, 2015.

[26] R. Vijay, M. Devoret, and I. Siddiqi, "Invited review article: The josephson bifurcation amplifier," *Review of Scientific Instruments*, vol. 80, no. 11, p. 111101, 2009.

[27] X. Zhou, V. Schmitt, P. Bertet, D. Vion, W. Wustmann, V. Shumeiko, and D. Estève, "High-gain weakly nonlinear flux-modulated josephson parametric amplifier using a squid array," *Physical Review B*, vol. 89, no. 21, p. 214517, 2014.

[28] T. Palomaki, J. Harlow, J. Teufel, R. Simmonds, and K. W. Lehnert, "Coherent state transfer between itinerant microwave fields and a mechanical oscillator," *Nature*, vol. 495, no. 7440, p. 210, 2013.

[29] X. Zhou, D. Cattiaux, R. Gazizulin, A. Luck, O. Maillet, T. Crozes, J.-F. Motte, O. Bourgeois, A. Fefferman, and E. Collin, "On-chip thermometry for microwave optomechanics implemented in a nuclear demagnetization cryostat," *Physical Review Applied*, vol. 12, no. 4, p. 044066, 2019.

[30] F. Massel, T. Heikkilä, J.-M. Pirkkalainen, S.-U. Cho, H. Saloniemi, P. J. Hakonen, and M. A. Sillanpää, "Microwave amplification with nanomechanical resonators," *Nature*, vol. 480, no. 7377, p. 351, 2011.

[31] D. M. Pozar, *Microwave engineering*. John wiley & sons, 2009.

[32] J. Sulkko, M. A. Sillanpaa, P. Hakkinen, L. Lechner, M. Helle, A. Fefferman, J. Parpia, and P. J. Hakonen, "Strong gate coupling of high-q nanomechanical resonators," *Nano letters*, vol. 10, no. 12, pp. 4884–4889, 2010.

[33] M. A. Sillanpää, J. Sarkar, J. Sulkko, J. Muhonen, and P. J. Hakonen, "Accessing nanomechanical resonators via a fast microwave circuit," *Applied Physics Letters*, vol. 95, no. 1, p. 011909, 2009.

[34] A. Weinstein, C. Lei, E. Wollman, J. Suh, A. Metelmann, A. Clerk, and K. Schwab, "Observation and interpretation of motional sideband asymmetry in a quantum electromechanical device," *Physical Review X*, vol. 4, no. 4, p. 041003, 2014.

[35] I. Golokolenov, D. Cattiaux, S. Kumar, M. Sillanpää, L. Mercier de Lépinay, A. Fefferman, and E. Collin, "Microwave optomechanics in the classical regime," *arXiv:2011.13814*.

[36] X. Zhou, D. Cattiaux, D. Theron, and E. Collin, "Electric circuit model of microwave optomechanics," *Journal of Applied Physics*, vol. 129, no. 11, p. 114502, 2021.

[37] L. Spietz, K. Lehnert, I. Siddiqi, and R. Schoelkopf, "Primary electronic thermometry using the shot noise of a tunnel junction," *Science*, vol. 300, no. 5627, pp. 1929–1932, 2003.

[38] F. Hocke, X. Zhou, A. Schliesser, T. J. Kippenberg, H. Huebl, and R. Gross, "Electromechanically induced absorption in a circuit nano-electromechanical system," *New Journal of Physics*, vol. 14, no. 12, p. 123037, 2012.

[39] S. Weis, R. Rivière, S. Deléglise, E. Gavartin, O. Arcizet, A. Schliesser, and T. J. Kippenberg, "Optomechanically induced transparency," *Science*, vol. 330, no. 6010, pp. 1520–1523, 2010.

[40] S. Kumar, D. Cattiaux, E. Collin, A. Fefferman, and X. Zhou, "Microwave optomechanically induced transparency and absorption between 250 and 450 mk," *Journal of Low Temperature Physics*, vol. 210, no. 5, pp. 562–572, 2023.

[41] S. E. Lyshevski, *MEMS and NEMS: systems, devices, and structures*. CRC press, 2018.

[42] A. Bachtold, J. Moser, and M. I. Dykman, "Mesoscopic physics of nanomechanical systems," *Rev. Mod. Phys.*, vol. 94, p. 045005, Dec 2022.

[43] O. Maillet, X. Zhou, R. Gazizulin, A. M. Cid, M. Defoort, O. Bourgeois, and E. Collin, "Nonlinear frequency transduction of nanomechanical brownian motion," *Physical Review B*, vol. 96, no. 16, p. 165434, 2017.

[44] O. Maillet, D. Cattiaux, X. Zhou, R. R. Gazizulin, O. Bourgeois, A. D. Fefferman, and E. Collin, "Nanomechanical damping via electron-assisted relaxation of two-level systems," *Physical Review B*, vol. 107, no. 6, p. 064104, 2023.

[45] I. Golokolenov, A. Ranadive, L. Planat, M. Esposito, N. Roch, X. Zhou, A. Fefferman, and E. Collin, "Thermodynamics of a single mesoscopic phononic mode," *Physical Review Research*, vol. 5, no. 1, p. 013046, 2023.

[46] M. Spletzer, A. Raman, A. Q. Wu, X. Xu, and R. Reifenberger, "Ultrasensitive mass sensing using mode localization in coupled microcantilevers," *Applied Physics Letters*, vol. 88, no. 25, p. 254102, 2006.

[47] M. Spletzer, A. Raman, H. Sumali, and J. P. Sullivan, "Highly sensitive mass detection and identification using vibration localization in coupled microcantilever arrays," *Applied Physics Letters*, vol. 92, no. 11, p. 114102, 2008.

[48] Y.-T. Yang, C. Callegari, X. Feng, K. L. Ekinci, and M. L. Roukes, "Zeptogram-scale nanomechanical mass sensing," *Nano letters*, vol. 6, no. 4, pp. 583–586, 2006.

[49] J. Chaste, A. Eichler, J. Moser, G. Ceballos, R. Rurali, and A. Bachtold, "A nanomechanical mass sensor with yoctogram resolution," *Nature nanotechnology*, vol. 7, no. 5, pp. 301–304, 2012.

[50] R. Gazizulin, O. Maillet, X. Zhou, A. M. Cid, O. Bourgeois, and E. Collin, "Surface-induced near-field scaling in the knudsen layer of a rarefied gas," *Physical Review Letters*, vol. 120, no. 3, p. 036802, 2018.

[51] D. N. Guerra, A. R. Bulsara, W. L. Ditto, S. Sinha, K. Murali, and P. Mohanty, "A noise-assisted reprogrammable nanomechanical logic gate," *Nano letters*, vol. 10, no. 4, pp. 1168–1171, 2010.

[52] I. Mahboob, E. Flurin, K. Nishiguchi, A. Fujiwara, and H. Yamaguchi, "Interconnect-free parallel logic circuits in a single mechanical resonator," *Nature communications*, vol. 2, no. 1, pp. 1–7, 2011.

[53] R. Karabalin, R. Lifshitz, M. Cross, M. Matheny, S. Masmanidis, and M. Roukes, "Signal amplification by sensitive control of bifurcation topology," *Physical review letters*, vol. 106, no. 9, p. 094102, 2011.

[54] I. Mahboob and H. Yamaguchi, "Bit storage and bit flip operations in an electromechanical oscillator," *Nature nanotechnology*, vol. 3, no. 5, pp. 275–279, 2008.

[55] H. Okamoto, A. Gourgout, C.-Y. Chang, K. Onomitsu, I. Mahboob, E. Y. Chang, and H. Yamaguchi, "Coherent phonon manipulation in coupled mechanical resonators," *Nature Physics*, vol. 9, no. 8, pp. 480–484, 2013.

[56] T. Faust, J. Rieger, M. J. Seitner, P. Krenn, J. P. Kotthaus, and E. M. Weig, "Nonadiabatic dynamics of two strongly coupled nanomechanical resonator modes," *Physical review letters*, vol. 109, no. 3, p. 037205, 2012.

[57] F. D. Bannon, J. R. Clark, and C.-C. Nguyen, "High-q hf microelectromechanical filters," *IEEE Journal of solid-state circuits*, vol. 35, no. 4, pp. 512–526, 2000.

[58] T. Faust, J. Rieger, M. J. Seitner, J. P. Kotthaus, and E. M. Weig, "Coherent control of a classical nanomechanical two-level system," *Nature Physics*, vol. 9, no. 8, pp. 485–488, 2013.

[59] I. Mahboob, K. Nishiguchi, H. Okamoto, and H. Yamaguchi, "Phonon-cavity electromechanics," *Nature Physics*, vol. 8, no. 5, pp. 387–392, 2012.

[60] F. Sun, X. Dong, J. Zou, M. I. Dykman, and H. B. Chan, "Correlated anomalous phase diffusion of coupled phononic modes in a sideband-driven resonator," *Nature communications*, vol. 7, no. 1, pp. 1–8, 2016.

[61] T. Faust, P. Krenn, S. Manus, J. P. Kotthaus, and E. M. Weig, "Microwave cavity-enhanced transduction for plug and play nanomechanics at room temperature," *Nature communications*, vol. 3, no. 1, pp. 1–6, 2012.

[62] D. Cattiaux, X. Zhou, S. Kumar, I. Golokolenov, R. Gazizulin, A. Luck, L. M. de Lépinay, M. Sillanpää, A. Armour, A. Fefferman, *et al.*, "Beyond linear coupling in microwave optomechanics," *Physical Review Research*, vol. 2, no. 3, p. 033480, 2020.

[63] Q. Zeng and K. Zeng, "Strong phonon-cavity coupling and parametric interaction in a single microcantilever under ambient conditions," *Journal of Physics D: Applied Physics*, vol. 54, no. 47, p. 475307, 2021.

[64] L. Fan, K. Y. Fong, M. Poot, and H. X. Tang, "Cascaded optical transparency in multimode-cavity optomechanical systems," *Nature communications*, vol. 6, no. 1, pp. 1–6, 2015.

[65] S. Shahidani, M. Naderi, and M. Soltanolkotabi, "Control and manipulation of electromagnetically induced transparency in a nonlinear optomechanical system with two movable mirrors," *Physical Review A*, vol. 88, no. 5, p. 053813, 2013.

[66] I. Mahboob, N. Perrissin, K. Nishiguchi, D. Hatanaka, Y. Okazaki, A. Fujiwara, and H. Yamaguchi, "Dispersive and dissipative coupling in a micromechanical resonator embedded with a nanomechanical resonator," *Nano letters*, vol. 15, no. 4, pp. 2312–2317, 2015.

[67] R. Karabalin, M. Cross, and M. Roukes, "Nonlinear dynamics and chaos in two coupled nanomechanical resonators," *Physical Review B*, vol. 79, no. 16, p. 165309, 2009.

[68] R. De Alba, F. Massel, I. R. Storch, T. Abhilash, A. Hui, P. L. McEuen, H. G. Craighead, and J. M. Parpia, "Tunable phonon-cavity coupling in graphene membranes," *Nature nanotechnology*, vol. 11, no. 9, pp. 741–746, 2016.

[69] M. Šiškins, E. Sokolovskaya, M. Lee, S. Mañas-Valero, D. Davidovikj, H. S. J. van der Zant, and P. G. Steeneken, "Tunable strong coupling of mechanical resonance between spatially separated feps3 nanodrums," *Nano letters*, vol. 22, no. 1, pp. 36–42, 2021.

[70] P. Huang, P. Wang, J. Zhou, Z. Wang, C. Ju, Z. Wang, Y. Shen, C. Duan, and J. Du, "Demonstration of motion transduction based on parametrically coupled mechanical resonators," *Physical Review Letters*, vol. 110, no. 22, p. 227202, 2013.

[71] X. Zhou, S. Venkatachalam, R. Zhou, H. Xu, A. Pokharel, A. Fefferman, M. Zaknoune, and E. Collin, "High-q silicon nitride drum resonators strongly coupled to gates," *Nano Letters*, vol. 21, no. 13, pp. 5738–5744, 2021.

[72] J. Hertzberg, T. Rocheleau, T. Ndukum, M. Savva, A. A. Clerk, and K. Schwab, "Back-action-evading measurements of nanomechanical motion," *Nature Physics*, vol. 6, no. 3, pp. 213–217, 2010.

[73] H. Xu, S. Venkatachalam, C. Boyaval, P. Tilmant, F. Vaurette, Y. Deblock, D. Theron, and X. Zhou, "Fabrication of silicon nitride membrane nanoelectromechanical resonator," *Microelectronic Engineering*, vol. 280, p. 112064, 2023.

[74] D. Garcia-Sanchez, A. M. van der Zande, A. S. Paulo, B. Lassagne, P. L. McEuen, and A. Bachtold, "Imaging mechanical vibrations in suspended graphene sheets," *Nano letters*, vol. 8, no. 5, pp. 1399–1403, 2008.

[75] D. Hälg, T. Gisler, Y. Tsaturyan, L. Catalini, U. Grob, M.-D. Krass, M. Héritier, H. Mattiat, A.-K. Thamm, R. Schirhagl, *et al.*, "Membrane-based scanning force microscopy," *Physical Review Applied*, vol. 15, no. 2, p. L021001, 2021.

[76] J. Rieger, A. Isacsson, M. J. Seitner, J. P. Kotthaus, and E. M. Weig, "Energy losses of nanomechanical resonators induced by atomic force microscopy-controlled mechanical impedance mismatching," *Nature communications*, vol. 5, no. 1, p. 3345, 2014.

[77] D. Garcia-Sanchez, A. San Paulo, M. J. Esplandiu, F. Perez-Murano, L. Forró, A. Aguasca, and A. Bachtold, "Mechanical detection of carbon nanotube resonator vibrations," *Physical review letters*, vol. 99, no. 8, p. 085501, 2007.

[78] T. Barois, A. Ayari, A. Siria, S. Perisanu, P. Vincent, P. Poncharal, and S. Purcell, "Ohmic electromechanical dissipation in nanomechanical cantilevers," *Physical Review B*, vol. 85, no. 7, p. 075407, 2012.

[79] I. Tsioutsios, A. Tavernarakis, J. Osmond, P. Verlot, and A. Bachtold, "Real-time measurement of nanotube resonator fluctuations in an electron microscope," *Nano letters*, vol. 17, no. 3, pp. 1748–1755, 2017.

[80] H. Huber, M. Moertelmaier, T. Wallis, C. Chiang, M. Hochleitner, A. Imtiaz, Y. Oh, K. Schilcher, M. Dieudonne, J. Smoliner, *et al.*, "Calibrated nanoscale capacitance measurements using a scanning microwave microscope," *Review of Scientific Instruments*, vol. 81, no. 11, 2010.

[81] S. Gu, X. Zhou, T. Lin, H. Happy, and T. Lasri, "Broadband non-contact characterization of epitaxial graphene by near-field microwave microscopy," *Nanotechnology*, vol. 28, no. 33, p. 335702, 2017.

[82] A. Pokharel, H. Xu, S. Venkatachalam, E. Collin, and X. Zhou, "Coupling capacitively distinct mechanical resonators for room-temperature phonon-cavity electromechanics," *Nano Letters*, vol. 22, no. 18, pp. 7351–7357, 2022.

[83] K. Y. Fong, H.-K. Li, R. Zhao, S. Yang, Y. Wang, and X. Zhang, "Phonon heat transfer across a vacuum through quantum fluctuations," *Nature*, vol. 576, no. 7786, pp. 243–247, 2019.

[84] Z. Xu, X. Gao, J. Bang, Z. Jacob, and T. Li, "Non-reciprocal energy transfer through the casimir effect," *Nature nanotechnology*, vol. 17, no. 2, pp. 148–152, 2022.

[85] H. Xu, S. Venkatachalam, T.-H. Rabenimanana, C. Boyaval, S. Eliet, F. Braud, E. Collin, D. Theron, and X. Zhou, "Imaging nanomechanical vibrations and manipulating parametric mode coupling via scanning microwave microscopy," *Nano Letters*, vol. 24, no. 28, pp. 8550–8557, 2024.

[86] B. Hauer, C. Doolin, K. Beach, and J. Davis, "A general procedure for thermomechanical calibration of nano/micro-mechanical resonators," *Annals of Physics*, vol. 339, pp. 181–207, 2013.

[87] A. Descombin, S. Perisanu, P. Poncharal, P. Vincent, S. Purcell, and A. Ayari, "Sensing and cooling of a nanomechanical resonator with an electron beam stimulated internal feedback and a capacitive force," *Journal of Applied Physics*, vol. 124, no. 6, 2018.

[88] S. Venkatachalam and X. Zhou, "Effects of stochastic forces on the nonlinear behaviour of a silicon nitride membrane nanoelectromechanical resonator," *Nanotechnology*, vol. 34, no. 21, p. 215202, 2023.

[89] D. Davidovikj, J. J. Slim, S. J. Cartamil-Bueno, H. S. Van Der Zant, P. G. Steeneken, and W. J. Venstra, "Visualizing the motion of graphene nanodrums," *Nano letters*, vol. 16, no. 4, pp. 2768–2773, 2016.

[90] J. Rieger, T. Faust, M. J. Seitner, J. P. Kotthaus, and E. M. Weig, "Frequency and q factor control of nanomechanical resonators," *Applied Physics Letters*, vol. 101, no. 10, 2012.

[91] M. Imboden and P. Mohanty, "Dissipation in nanoelectromechanical systems," *Physics Reports*, vol. 534, no. 3, pp. 89–146, 2014.

[92] A. Lazarus, T. Barois, S. Perisanu, P. Poncharal, P. Manneville, E. De Langre, S. Purcell, P. Vincent, and A. Ayari, "Simple modeling of self-oscillations in nanoelectromechanical systems," *Applied Physics Letters*, vol. 96, no. 19, p. 193114, 2010.

[93] D. Cattiaux, I. Golokolenov, S. Kumar, M. Sillanpää, L. Mercier de Lépinay, R. Gazizulin, X. Zhou, A. Armour, O. Bourgeois, A. Fefferman, *et al.*, "A macroscopic object passively cooled into its quantum ground state of motion beyond single-mode cooling," *Nature communications*, vol. 12, no. 1, pp. 1–6, 2021.

[94] K. Juliusson, S. Bernon, X. Zhou, V. Schmitt, H. Le Sueur, P. Bertet, D. Vion, M. Mirrahimi, P. Rouchon, and D. Esteve, "Manipulating fock states of a harmonic oscillator while preserving its linearity," *Physical Review A*, vol. 94, no. 6, p. 063861, 2016.

[95] B. Zwickl, W. Shanks, A. Jayich, C. Yang, A. Bleszynski Jayich, J. Thompson, and J. Harris, "High quality mechanical and optical properties of commercial silicon nitride membranes," *Applied Physics Letters*, vol. 92, no. 10, p. 103125, 2008.

[96] S. S. Verbridge, J. M. Parpia, R. B. Reichenbach, L. M. Bellan, and H. G. Craighead, "High quality factor resonance at room temperature with nanostrings under high tensile stress," *Journal of Applied Physics*, vol. 99, no. 12, p. 124304, 2006.

[97] V. Adiga, B. Ilic, R. Barton, I. Wilson-Rae, H. G. Craighead, and J. Parpia, "Modal dependence of dissipation in silicon nitride drum resonators," *Applied Physics Letters*, vol. 99, no. 25, p. 253103, 2011.

[98] Q. P. Unterreithmeier, T. Faust, and J. P. Kotthaus, "Damping of nanomechanical resonators," *Physical review letters*, vol. 105, no. 2, p. 027205, 2010.

[99] F. Massel, T. Heikkilä, J.-M. Pirkkalainen, S.-U. Cho, H. Saloniemi, P. J. Hakonen, and M. A. Sillanpää, "Microwave amplification with nanomechanical resonators," *Nature*, vol. 480, no. 7377, pp. 351–354, 2011.

[100] Q. P. Unterreithmeier, E. M. Weig, and J. P. Kotthaus, "Universal transduction scheme for nanomechanical systems based on dielectric forces," *Nature*, vol. 458, no. 7241, pp. 1001–1004, 2009.

[101] M. Abuwasib, P. Krantz, and P. Delsing, "Fabrication of large dimension aluminum air-bridges for superconducting quantum circuits," *Journal of Vacuum Science & Technology B, Nanotechnology and Microelectronics: Materials, Processing, Measurement, and Phenomena*, vol. 31, no. 3, p. 031601, 2013.

[102] P.-L. Yu, T. Purdy, and C. Regal, "Control of material damping in high-q membrane microresonators," *Physical review letters*, vol. 108, no. 8, p. 083603, 2012.

[103] V. P. Adiga, B. Ilic, R. Barton, I. Wilson-Rae, H. Craighead, and J. Parpia, "Approaching intrinsic performance in ultra-thin silicon nitride drum resonators," *Journal of Applied Physics*, vol. 112, no. 6, p. 064323, 2012.

[104] J. Lee, Z. Wang, K. He, J. Shan, and P. X.-L. Feng, "High frequency mos2 nanomechanical resonators," *ACS nano*, vol. 7, no. 7, pp. 6086–6091, 2013.

[105] D. Cattiaux, S. Kumar, X. Zhou, A. Fefferman, and E. Collin, "Geometrical nonlinearity of circular plates and membranes: An alternative method," *Journal of Applied Physics*, vol. 128, no. 10, p. 104501, 2020.

[106] G. Guisbiers, S. Strehle, O. Van Overschelde, and M. Wautelet, "Residual stresses in ta, mo, al and pd thin films deposited by e-beam evaporation process on si and si/sio2 substrates," in *AIP Conference Proceedings*, vol. 817, pp. 317–324, American Institute of Physics, 2006.